Advances in Space Radiation Physics and Transport

John W. Norbury[a], Tony C. Slaba[a], Sukesh Aghara[b], Francis F. Badavi[c], Steve R. Blattnig[a], Martha S. Clowdsley[a], Lawrence H. Heilbronn[d], Khin M. Maung[e], Christopher J. Mertens[a], Jack Miller[f], Ryan B. Norman[a], Chris A. Sandridge[a], Robert Singleterry[a], Nikolai Sobolevsky[g], Jan L. Spangler[h], Lawrence W. Townsend[d], Charles M. Werneth[a], John W. Wilson[c], Sharon Xiaojing Xu[a], Cary Zeitlin[i]

[a]*NASA Langley Research Center, Hampton, Virginia 23681, USA*
[b]*University of Massachusetts, Lowell, Massachusetts 01854, USA*
[c]*Old Dominion University, Norfolk, Virginia 23529, USA*
[d]*University of Tennessee, Knoxville, Tennessee 37996, USA*
[e]*University of Southern Mississippi, Hattiesburg, Mississippi 39406, USA*
[f]*Lawrence Berkeley National Laboratory, Berkeley, California 94720, USA*
[g]*Institute for Nuclear Research of the Russian Academy of Sciences, Moscow, Russia*
[h]*Science and Technology Corporation, Hampton, Virginia 23666, USA*
[i]*Leidos Innovations Corporation, Houston, Texas 77058, USA*

Keywords: Space radiation; Transport methods; Galactic cosmic rays

Abstract

The space radiation environment is a complex mixture of particle types and energies originating from sources inside and outside of the galaxy. These environments may be modified by the heliospheric and geomagnetic conditions as well as planetary bodies and vehicle or habitat mass shielding. In low Earth orbit (LEO), the geomagnetic field deflects a portion of the galactic cosmic rays (GCR) and all but the most intense solar particle events (SPE). There are also dynamic belts of trapped electrons and protons with low to medium energy and intense particle count rates. In deep space, the GCR exposure is more severe than in LEO and varies inversely with solar activity. Unpredictable solar storms also present an acute risk to astronauts if adequate shielding is not provided. Near planetary surfaces such as the Earth, moon or Mars, secondary particles are produced when the ambient deep space radiation environment interacts with these surfaces and/or atmospheres. These secondary particles further complicate the local radiation environment and modify the associated health risks. Characterizing the radiation fields in this vast array of scenarios and environments is a challenging task and is currently accomplished with a combination of computational models and dosimetry. The computational tools include models for the ambient space radiation environment, mass shielding geometry, and atomic and nuclear interaction parameters. These models are then coupled to a radiation transport code to describe the radiation field at the location of interest within a vehicle or habitat. Many new advances in these models have been made in the last decade, and the present review article focuses on the progress and contributions made by workers and collaborators at NASA in the same time frame. Although great progress has been made, and models continue to improve, significant gaps remain and are discussed in the context of planned future missions. Of particular interest is the juxtaposition of various review committee findings regarding the accuracy and gaps of combined space radiation environment, physics, and transport models with the progress achieved over the past decade. While current models are now fully capable of characterizing radiation environments in the broad range of forecasted mission scenarios, it should be remembered that uncertainties still remain and need to be addressed.

Contents

1 Introduction

Accurately characterizing the space radiation environment encountered by astronauts is a critical component of mission planning, shield design and optimization, and risk assessment. The current approach for quantifying exposure levels at NASA utilizes a combination of dosimetry and other space weather assets coupled with computational model evaluations. Mission planning and shield design, in particular, rely heavily on computational models since dosimetry is unavailable for the scenarios and architectures being considered. In-flight assessments rely mainly on dosimetry, but approaches that combine real-time measurements with model evaluations have been developed to estimate acute biological risks from solar storms (Mertens et al., 2018).

Although details vary for different mission scenarios, exposure estimates from a combined set of models are obtained using the following general approach. First, the ambient radiation field impinging on the mass shielding geometry or location of interest is described. This description usually comes in the form of particle flux or fluence as a function of kinetic energy for each particle type in the ambient field. As an example, in the case of solar particle events (SPE), there are various parameterizations (Townsend et al., 2018) for historical events that provide the proton fluence as a function of kinetic energy. Second, the relevant shielding geometry is described. In most cases, this simply includes the vehicle or habitat mass and human tissue shielding, but may also include other complicating factors such as the terrestrial surface and atmosphere (in the case of the moon and/or Mars). Third, models that describe atomic and nuclear interactions between the incoming ambient field and intervening material(s) are selected and must cover the full range of energies and particle types of relevance. These components are then input into a radiation transport code which describes how the ambient radiation field, or boundary condition, is modified as it propagates through the geometric definitions. The fundamental output from a radiation transport code is the particle flux or fluence as a function of kinetic energy, although other exposure quantities such as dose may also be calculated. These quantities are defined mathematically in the next paragraph.

Deterministic transport codes, such as HZETRN (High Z and Energy TRaNsport) developed at NASA Langley Research Center are based on solutions to the Boltzmann transport equation and are therefore highly efficient for space applications. Monte Carlo simulation codes, on the other hand, track individual particle trajectories and count specific events to determine output quantities of interest. In both deterministic and Monte Carlo codes, a fundamental output is the differential fluence ϕ (units cm^{-2} MeV^{-1}), for particle type i, with kinetic energy E (MeV), at a given location x.

Dose (at point x) is defined as

$$D(x) \equiv \sum_i \int_0^\infty dE\, S_i(E)\, \phi_i(x, E)\,, \tag{1}$$

where the sum includes all the different particle species. The units of dose are Gray

(Gy) defined as a Joule per kilogram (Gy $\equiv$ J/kg). Dose is a physical quantity expressing the amount of energy deposited at a point, x. However, different radiation particle types, i, produce different biological effects. One way of capturing such biological effects is through the use of a quality factor, $Q(L_i)$, which relates the biological effect to the linear energy transfer (LET). Thus, dose equivalent (at point x), in units of Sievert (Sv), is defined (ICRP, 1991; 2007) as

$$H(x) \equiv \sum_i \int_0^\infty dE\, Q(L_i(E))\, L_i(E)\, \phi_i(x,E)\ , \tag{2}$$

where the linear energy transfer (LET) is $L_i \equiv \frac{dE}{dx} \approx S_i(E)$, which is approximately equal to the stopping power. Effective dose (also units of Sv) is defined (ICRP, 1991; 2007) as a sum over all tissues (T),

$$E \equiv \sum_T w_T\, H_T\ , \tag{3}$$

where w_T are tissue weighting factors, reflecting the degree of radiation sensitivity of individual tissues, and H_T is the dose equivalent in each tissue. Dose equivalent and the associated quality factor are usually reserved for stochastic, relatively late occurring end-points such as cancer. However, deterministic effects refer to acute end-points such as hair loss, vomiting, or erythema which can be disabling during a mission. Hence, the gray equivalent (G), for tissue T, is a deterministic quantity defined as (NCRP, 2002)

$$G_T \equiv RBE_i\ D_T\ , \tag{4}$$

where RBE_i is the relative biological effectiveness of particle i, and D_T is the average absorbed dose in a tissue. Values for RBE_i are given in Table 2.2 of reference (NCRP, 2002).

Clearly, the model-based approach to radiation field characterization relies on several individual models, each of which have their own degree of uncertainty, reliability, and range of applicability. The uncertainty associated with these end-to-end model evaluations has been discussed in various publications and review committee findings. It is particularly interesting to consider some of the more recent review committee findings, as they generally summarize best-available knowledge and subject matter expert opinion. The International Commission on Radiological Protection (ICRP) make the following comments regarding the importance of radiation transport codes:

> *"Radiation transport calculations are important tools for information about radiation exposure of astronauts. Based on data about the primary radiation fields, transport calculations are able to calculate radiation fields inside a spacecraft, on the body of astronauts, and in organs or tissues of anthropomorphic phantoms."* (ICRP, 2013).

The ICRP states in the same document:

> *"The physics at the basis of the particle transport and cross-sectional data tables must be improved to further develop the computational methods. There is a lack of experimental cross section data for light fragments and neutrons. Codes need to be improved to treat all primary and secondary cascades including photons, protons, light ions, heavy ions, mesons, and electromagnetic cascades. The nuclear interaction database needs to be updated, especially for neutrons and light ions."* (ICRP, 2013).

The National Council on Radiation Protection and Measurements (NCRP) provide the following recommendations for improved galactic cosmic ray (GCR) models and radiation transport codes:

> *"Continue to update space environmental models as new data become available, and evaluate the role of pions and electromagnetic cascades in transport code predictions. Depending on the magnitude of pion and electromagnetic cascade products to the REID, radiobiology experiments to understand their effectiveness in contributing to radiation cancer risks may be warranted to reduce uncertainties."* (NCRP, 2014).

Finally, in their review of the NASA cancer risk model (Cucinotta et al., 2013) the National Research Council (NRC) makes the following comment regarding GCR environmental models:

> *"The primary uncertainty in the GCR environment calculation comes from a lack of understanding of the physical conditions of transport and the use of statistically based models. ... Having just passed through an unexpected historically deep solar minimum, it is clear that environmental uncertainties increase with time over years to decades. ... The recent incorporation of the CREME96 (Tylka et al., 1997) and Nymmik (Nymmik et al., 1996) models adds more complication, but basically tweaks the Badhwar-ONeill model to try to make more physical the variation of the modulation parameter Φ. However, there is no simple parameterization of the current models that yields the 22-year effects except in an ad hoc manner. The NASA GCR model could be improved by incorporating the 22-year-cycle variation."* (NRC, 2012).

The NRC also recommends:

> *" ... it is concluded that there have been reasonable advances in developing the predictive capability of radiation transport codes used in the NASA cancer risk assessment. However, it is noted that comparisons of HZETRN with spaceflight measurements still show greater than 20 percent difference for several occasions ... the continuous collection of data for different shielding materials and different ion beams is recommended for further validation of transport code, especially for thick targets. The 2011 NASA report also states that the cross-section data are sparse for some projectile-target combinations, especially above 1,000 MeV/u, and*

improvements are required in how differential cross sections are represented in transports. The committee agrees with this point and suggests that NASA continue compiling experimental thick-target data for code validation." (NRC, 2012).

These various review committee findings generally suggest that although combined models have greatly improved in recent years and appear capable of characterizing radiation fields over the broad range of missions being considered, significant uncertainties remain that should be addressed. In this paper, research conducted in the areas of space radiation environments, nuclear physics, and radiation transport by investigators and collaborators working at NASA from ∼2005 to almost present day is reviewed.

This paper is organized to mirror the workflow of most radiation analyses. The major components of the ambient space radiation environment are covered first, followed by discussion of nuclear physics and interactions. Radiation transport procedures are then described, and finally, integrated tool sets that combine best practice methods into easy-to-use web-interfaces and other applications are highlighted. In each section, an overview of the accomplishments and impact is provided. Emphasis on verification, validation, and uncertainty quantification is apparent throughout the paper, as these were used to guide research directions and communicate progress. The paper finishes with a section of "Highlighted Applications" (Section 5), which uses the research of the previous sections in applications which have represented some of the most important recent advances in space radiation physics and transport.

2 Ambient Space Radiation Environment

2.1 Galactic Cosmic Rays

The GCR environment is comprised of approximately 87% protons, 12% helium, and the remaining 1% is covered by heavier ions from lithium up through uranium and beyond (Simpson, 1983). Over a given time period, the energy spectrum for each of these particles has a peak intensity near ∼300 MeV/n. The GCR are inversely correlated with solar activity so that at solar maximum, the GCR intensity is at a minimum, and at solar minimum, the GCR intensity is maximal. Knowledge of the GCR composition and energy spectrum has been derived from various measurements obtained from high altitude balloon flights, satellites, and detectors flying onboard the Shuttle or International Space Station (ISS). Despite the knowledge gained, the available measurement database is insufficient to fully characterize the energy distribution for each particle type as a function of time in the solar cycle. Models were therefore needed to describe the GCR spectrum for all particle types and energies of relevance to space radiation protection.

By 2005, several GCR environment models developed for space radiation pro-

tection applications were readily available (Nymmik et al., 1996; O'Neill, 2006, 2010). These models were largely empirical or semi-empirical and simultaneously calibrated to and validated against the same measurement database (i.e. same data being used to calibrate model and then quantify model uncertainty). Updates to the Badhwar-O'Neill (BON) GCR model revealed limitations of the coupled calibration/validation development efforts as well as limitations of the available space flight measurements. Figure 1 shows the effective dose as a function of time for a female astronaut behind 20 g/cm^2 of aluminum shielding using three different versions of the BON model to generate the boundary condition GCR spectra. For the 1977 solar minimum, it can be seen that switching from BON2004 to BON2010 reduced the effective dose by ∼35%. Subsequently updating from BON2010 to BON2011 then increased the effective dose by ∼25%. Even larger variations were found at other time points. Although model updates are expected to modify such exposure estimates, of particular concern here was that no new space flight measurements were obtained or considered between 2004 and 2011, yet the quoted uncertainty of each model version was within 15% or less despite significantly larger version-to-version differences as shown in Figure 1.

As a result of these changes, Slaba and Blattnig (2014a) began considering possible improvements to the calibration and validation procedures applied to the GCR models. The first step was to quantify the relative importance of each ion and energy in the ambient GCR field to exposure quantities of interest for space radiation applications. Table 1 shows the fraction of effective dose induced behind shielding by boundary GCR ions and energies (i.e. the particle and energy impinging externally on the shield geometry). It can be seen in the table that GCR ions with charge, Z, greater than 2 and energies below 500 MeV/n induce less than 5% of the effective dose behind shielding. This finding was particularly important since most of the GCR models at that time were developed and validated against Advanced Composition Explorer/Cosmic Ray Isotope Spectrometer (ACE/CRIS) measurements[1] taken below 500 MeV/n. In other words, the GCR models developed for space radiation protection were calibrated and validated against measurements covering particles and energies having only a minor impact on relevant space radiation exposure quantities.

Subsequent studies focused on developing efficient uncertainty propagation methods (Slaba and Blattnig, 2014b) and rigorous validation approaches (Slaba et al., 2014c). The uncertainty propagation methods allowed GCR model uncertainty to be projected into effective dose estimates behind shielding in a computationally efficient manner, and the validation approaches focused on ion and energy groups of interest to space applications.

It was found that the BON2010 and Matthia (Matthia et al., 2013) models were of comparable accuracy and induced similar errors on effective dose behind shielding. Similar conclusions were reached by Mrigakshi et al. (2012) independently. Follow-

[1]ACE/CRIS database available at
http://www.srl.caltech.edu/ACE/ASC/level2/lvl2DATA_CRIS.html

ing this work, the tools developed by Slaba et al. (2014a-c) were used to directly re-calibrate the BON model with improved focus on the particle types and energies of interest to human spaceflight. This resulted in the BON2014 model (O'Neill et al., 2015). Figure 2 shows the relative uncertainty of various BON models along with the Matthia model. It can be seen that the recalibration implemented in BON2014 significantly reduced uncertainties for all particle types and energies compared to prior versions. Finally, Figure 3 shows a comparison of effective dose behind shielding using the BON2014 and Matthia GCR models. Much better agreement between the results is observed (average relative difference of ∼5%) and appears consistent with the uncertainty estimates shown in Figure 2.

Recently, Norman et al. (2016) compared available GCR models to measurements from the Radiation Dosimetry Experiment (RaD-X) balloon flights (Mertens, 2016). Norbury et al. (2018a) also compared available GCR models to the newly released measurements from the Alpha Magnetic Spectrometer II (AMS-II) instrument and the SINP GCR model (Kuznetsov et al., 2017). Although these studies generally conclude that current GCR models are reasonably accurate, continued efforts to validate and update GCR models will be important as exploration missions push beyond low Earth orbit (LEO). The recent AMS-II (Aguilar et al., 2018) and Payload for Anti-Matter/Matter Exploration and Light-nuclei Astrophysics (PAMELA) (Martucci et al., 2018) measurements of monthly proton and alpha flux rates will be particularly valuable given the previous lack of time-resolved measurements for these particles and that protons and alphas alone account for more than half of the exposure behind shielding (Slaba and Blattnig, 2014a). It is expected that recalibration of the currently available GCR models to the new measurements will further decrease uncertainties.

2.2 Solar Particle Events

For missions beyond LEO, there is a risk of exposure from solar particle events (SPE). The proton component of an SPE is the main concern for astronaut protection, although some events may contain helium isotopes and heavier nuclei. The spectral characteristics of SPE are widely varying but are usually described as low-to-medium energy (compared to GCR) with a majority of the protons having energy below hundreds of MeV and maximum energies in the GeV region. Intensities are also widely varying, with most events presenting a negligible concern to nominally shielded crew or instrumentation. Despite the variability, exposure to SPE for crew members with inadequate shielding or during extra vehicular activities (EVA) would present serious acute health risks and jeopardize mission objectives.

Current models are limited in their ability to adequately forecast the occurrence of an event, the likelihood of one or more events occurring in a given time period, or the spectral characteristics of an event if one occurs. Probabilistic models have been developed to address some of these issues (Xapsos et al., 1999; Feynman et al., 2002; Kim et al., 2009, 2017) but contain a large degree of uncertainty. Space

weather assets provide some level of nowcasting, but inferring total event duration and intensity given the onset of a storm remains challenging (Lovelace et al., 2018). Post-mission analysis for astronaut exposure record keeping is also hampered by the fact that satellite measurements are limited to energies having little impact on exposures behind shielding.

For managing in-flight risks, Mertens et al. (2018) have developed a method to integrate the capabilities of the HZETRN transport code (Slaba et al., 2010a,b) with Tylka's representation of historical ground level events (Tylka et al., 2010) and planned on-board dosimetry. This approach relies on real-time active dosimetry at several locations throughout a vehicle geometry to provide an indirect measure of spectral characteristics and intensity during an SPE. At a given time, the dosimeter values are compared to a pre-generated database of results calculated with HZETRN. Using regression techniques, the database entry that best-fits the dosimeter values is selected and appropriately scaled with measurement values for input to an acute biological effects model. In this way, the integrated system makes best use of available real-time dosimetry, historical knowledge of SPE spectral characteristics and efficient and validated computational tools such as HZETRN to estimate possible acute biological effects during a storm. This information may be used to inform crew members and possibly alter operational activities or begin storm shelter entry.

NASA previously adopted the SPE proton spectrum, as parameterized by King (1974) for the August 1972 event, as the design standard for the Orion Multi-Purpose Crew Vehicle (MPCV) (NASA, 2015). In its 2008 report, the NRC noted that the King parameterization for the 1972 event spectrum was not representative of a worst case event (NRC, 2008). Instead, the report recommended:

> *"The dose levels made possible by a shielding design should also be calculated using the observed proton spectrum from other large events in the historical record, even if it is not feasible to modify the shielding design as a result. The October 1989 event is particularly important in this regard."*

In January 2017, a technical interchange meeting was held at NASA Langley Research Center to develop storm shelter requirements for mission beyond LEO. The charge to the meeting participants was to *"Provide NASA recommendations for a design standard SPE that will be used to evaluate the adequacy of storm shelters for beyond LEO habitats."* A report of the meeting and the recommendations was recently published (Townsend et al., 2018). Discussions involving the meeting participants focused on a SPE design standard composed of the sum of the proton spectra from the October 1989 series of events, as modeled by Tylka et al. (2010) using Band function parameterizations that better model the high energy part of the spectrum. Figure 4 displays the summed spectra for the October 1989 series. Also displayed are spectra representing various confidence levels from a probabilistic model for a one year mission (Xapsos et al., 1999). Note that the Tylka model spectrum is comparable to the 90th percentile confidence level event for proton energies above 10 MeV.

The recommendations agreed upon by the meeting participants were (Townsend et al., 2018):

1. *"The habitat shall provide protection to ensure that gray equivalent to astronaut blood forming organs (BFO) does not exceed 250 mGy-Eq for the design SPE.*
2. *The proton energy spectrum in Table 2 of Townsend et al. (2018) shall be used as the design reference SPE environment.*
3. *If the protection system requires assembly and installation, it must take no more than 30 minutes.*
4. *Spacecraft protection systems shall be designed to ensure that astronaut radiation exposure is kept As Low As Reasonably Achievable (ALARA)."*

The rationale for the 250 mGy-Eq BFO dose limit is based on the permissible exposure limits in NASA Space Flight Human-System Standard Volume 1, Revision A: Crew Health (NASA, 2007). This limit is imposed to prevent clinically significant non-cancer tissue effects resulting from exposure to SPEs. Limiting the BFO exposure to 250 mGy-eq during any 30 day period is expected to drive a shield design, and thereby also ensure other permissible exposure limits for non-cancer tissue effects will not be exceeded.

The recommendation that the summed proton spectrum for the October 1989 series of SPEs be used as the design standard follows from its status as the most intense SPE environment occurring within a 30 day period during the era of satellite measurements. In addition, the combined environment is approximately equivalent to a 90 percentile event for a one year mission. The rationale for the requirement that assembly of a protection system be no more than 30 minutes is based upon consideration that historic SPEs have variable rise times and total durations; hence, it is possible that radiation exposures incurred before astronauts enter a shelter might exceed 250 mGy-Eq to BFO. However, requiring assembly time to be 30 minutes or less should ensure that there is a low probability of the dose limit being exceeded. Finally, the requirement that in-flight radiation exposure be maintained using the ALARA principle is still followed in the Permissible Exposure Limits in NASA Standard 3001 (NASA, 2007).

2.3 Low Earth Orbit

The LEO radiation environment is comprised of trapped electrons and protons, and a GCR spectrum which is attenuated by the geomagnetic field. The trapped particles result from the decay of atmospheric neutrons as they leak from the Earth's atmosphere into the trapping region. The average kinetic energy of the inner trapped electrons is a few hundred keV. These electrons are easily prevented from reaching the spacecraft interior by the slightest amount of shielding and are mainly of concern to an astronaut in a spacesuit during EVA, or for an externally mounted, lightly shielded electronics device. Trapped protons, on the other hand, can reach hundreds

of MeV and are therefore capable of reaching the interior of ISS or a shielded vehicle. These protons contribute to the astronaut exposure on ISS as it passes through the South Atlantic Anomaly (SAA) along its trajectory. The GCR environment in LEO is modified compared to free space as a result of geomagnetic shielding. Even highly energetic GCR ions with tens of GeV/n may be deflected, depending on the exact geographic location being considered. For mission analysis, astronaut recording keeping, shield design, and validation of integrated model sets (i.e. environment, radiation physics and transport, and mass shielding), LEO environment models must be capable of efficiently and accurately determining the trapped proton spectrum and attenuated GCR environment at any time and location near Earth.

The trapped particles in the geomagnetic field have been modeled from data obtained during two epochs of solar cycle 20 (solar minimum of 1965 and solar maximum of 1970), and are used with the geomagnetic fields on which the B and L maps were prepared (McCormack, 1988). The 1965 analysis, using the magnetic field model of Jensen and Cain (1962), resulted in the particle population maps AP8MIN (Sawyer and Vette, 1976). The 1970 analysis, using the magnetic field model of GSFC 12/66 (Cain et al., 1967) extended to 1970, resulted in the particle population maps of AP8MAX (Sawyer and Vette, 1976). To define an omni-directional and time dependent trapped proton model, AP8MIN/AP8MAX data were coupled to 50 years of F10.7 solar radio flux and neutron monitor measurements (Badavi et al., 2011). This provided an efficient computational tool by which exposures on Space Transportation System (STS: shuttle) and ISS can be calculated (Badavi et al., 2011). Recent work has focused on extending the omni-directional model to include angular dependence in the trapped proton spectral description (Badavi et al., 2015). When coupled to radiation transport codes and vehicle mass models, such efforts may provide an improved description of exposure estimate for near Earth applications.

Using this time-dependent trapped proton model along the equatorial plane, Figure 5 represents the differential flux rates for trapped protons as a function of energy and altitude (Badavi et al., 2013). It must be mentioned that the database for the trapped proton model (AP8MIN/AP8MAX) were developed in the 1970s and 1980s during solar quiet times and provide sufficient information for the shield design of a spacecraft. As a result, there are well known limitations on the validity of the AP8MIN/AP8MAX model, and over the past several years, a broad consensus is reached that the trapped environment, as quantified by the AP8MIN/AP8MAX model, requires a more accurate, comprehensive and up-to-date standard. The AP9 model is now available (Ginet et al., 2013); however, it does not currently support time-dependent analysis and therefore hinders its use in human exposure evaluation activities.

For the calculation of the LEO GCR environment, a transmission function, which depends on rigidity, R, is computed. The rigidity (momentum per unit charge) dependent transmission function is currently based on the combined work of Stormer (1937) and Smart and Shea (1983). This allows GCR transmission to be quickly

calculated at any point near Earth in any direction. Additional studies have been performed to replace the simplified Stormer model with more detailed models based on particle trajectory tracing algorithms (Smart and Shea, 2009). However, such models tend to be computationally expensive, thereby making their use in some applications difficult.

Validation and uncertainty quantification efforts usually focused on comparing models to measurements over the entirety of the ISS trajectory in a given time duration (Wilson et al., 2007). Although informative, such approaches are limited in their ability to identify systematic model errors and can be clouded by significant uncertainties associated with trapped proton environmental models.

To address this problem and avoid the shortcomings of trapped proton models, statistical validation studies were performed by Slaba et al. (2011a, 2013a) to examine LEO GCR model behavior as a function of vertical cutoff rigidity. The use of active dosimetry in these studies allowed a clear separation between LEO GCR and trapped proton contributions, and the LEO GCR data could then be further studied as a function of vertical cutoff rigidity and compared to model results with rigorous uncertainty quantification metrics.

These comparisons revealed a clear and systematic trend of the combined model under-predicting measurements, with decreasing errors as the cutoff rigidity was reduced (i.e. approaching high latitudes). The average model error when compared to measurement data over the entire ISS trajectory ranged from 20% - 30%, depending on the location of the dosimeter being considered. Errors ranged from 10% - 20% at the lowest cutoff rigidities (approaching free space conditions). Such trends are encouraging in the sense that model errors are reduced as environment conditions approach deep space, suggesting radiation analysis for mission beyond LEO are reasonably accurate. However, work is ongoing to resolve the discrepancies at higher cutoff rigidities.

2.4 Lunar Surface

The lunar surface radiation environment includes back-scattered, or albedo, particles produced by nuclear collisions between the incoming SPE protons or GCR ions and lunar regolith. Of the albedo particles produced (Hayatsu et al., 2008) neutrons present the main biological risk and were therefore carefully studied in various publications. Some agreement in the literature could be found that the albedo neutron contribution to total exposure in unshielded conditions was less than 10% for SPE and less than 20% for GCR. However, much larger variation was found when shielding was considered. These differences could be attributed to the usage of various environmental models, geometric configurations, transport codes, and conversion coefficients relating neutron fluence to effective dose.

Slaba et al. (2011b) further investigated lunar albedo neutron contributions in order to provide a more comprehensive and coherent picture in support of design and mission architecture studies. Included in the analysis were comparisons between the

bi-directional neutron transport released with HZETRN2010 (Slaba et al., 2010b) (discussed later in this paper) and various Monte Carlo simulation results, as shown in Figure 6. It can be seen that the HZETRN2010 results are in close agreement with the MC simulations over a broad range of energies, up to approximately 200 MeV. Recent studies by Heilbronn et al. (2015) have shown that this portion (< 200 MeV) of the neutron energy spectrum accounts for more than half of the biological neutron exposure in deep space.

The main result of this work is shown in Figure 7 which gives the albedo neutron contribution to effective dose on the lunar surface within shielding exposed to SPE and GCR environments. It can be seen that polyethylene shielding is highly effective in reducing the neutron exposure compared to aluminum. This is a result of elastic collisions occurring between neutrons and hydrogen within polyethylene, resulting in significant attenuation of the neutron field. In the case of SPE, the albedo neutron contribution is somewhat sensitive to spectral characteristics, as might be expected. While in the case of GCR, albedo neutron contributions appear more sensitive to shielding characteristics than time in the solar cycle (i.e. solar min vs. solar max).

2.5 Martian Surface

The Martian surface radiation environment is further complicated (compared to the moon) by the presence of a thin atmosphere. As incoming GCR or SPE ions interact with the atmosphere, secondary particles are produced in a manner loosely similar to what occurs on Earth. The mix of primary and secondary particles that reach the surface further interact with the soil and produce back-scattered neutrons (and other particles).

Measurements from the Mars curiosity rover Science Laboratory Radiation Detector (MSLRAD) have offered a unique opportunity to validate transport code predictions of the Martian surface environment. Moreover, broad interest from the scientific community has led to several inter-code comparisons so that differences between nuclear physics and transport models can be systematically investigated and hopefully resolved.

In Figure 8, results from Matthia et al. (2017) show the neutron and proton flux rates from MSLRAD and multiple transport codes. It can be seen in the figure that the codes agree very well on proton fluxes above $\sim$300 MeV, where values are dominated by primary GCR protons. Below 300 MeV, spectral results are more heavily influenced by secondary particle production occurring in the atmosphere. In this region, it is clear that significant variation in the nuclear physics models remains present and needs to be addressed. The neutron spectral results from this study are more difficult to interpret. In the special issue of LSSR in which the proceedings of a MSLRAD modeling workshop were published (Hassler et al., 2017), and Slaba and Stoffle (2017) showed that choice of GCR model or details of the atmospheric and regolith composition played a negligible role on predictions of surface quantities. Further, previous comparison of neutron spectra to MSLRAD

measurements (Matthia et al., 2016) did not show the same degree of variation, suggesting that choices in Monte Carlo model setup and normalization factors may be influencing results in Figure 8 more than uncertainties in nuclear physics models or transport code.

In general, it has been shown in the literature that models are in reasonable agreement with each other for nucleons and alphas at high energies. At lower energies, discrepancies have been observed and attributed to nuclear physics uncertainties. The lower energy nucleons contribute moderately to exposure behind shielding and should therefore be an important aspect of future research efforts. Isotopes of hydrogen and helium show even greater discrepancies across the energy domain (factors of 2 or more) and are similarly attributed to nuclear model uncertainty and large gaps in experimental databases (Norbury and Miller, 2012; Norbury et al., 2012).

Other investigations of the Mars surface environment have been conducted by Guo et al. (2017) who examined variations on dose associated with diurnal changes, atmospheric pressure and solar activity. Gronoff et al. (2015) and Norman et al. (2014) showed that atmospheric perturbations associated with dust storms have a small impact on surface exposure levels. Slaba et al. (2013b) also quantified the impact of aluminum and polyethylene shielding on the Martian surface as it relates to habitat design. Efforts to better understand the various factors influencing the Martian radiation environment should continue. Investigation of transport code uncertainty in the context of MSLRAD measurements and inter-code comparisons has been helpful in guiding future research and should also be pursued to close existing gaps.

3 Nuclear Physics

In the early development of HZETRN (∼1980s), efforts were mainly focused on developing efficient radiation transport procedures so that the scope of the GCR protection problem could be estimated. Nuclear fragmentation models were therefore needed to provide reasonable estimates for the dominant interactions occurring between GCR ions and intervening shield materials. Consequently, the NUCFRG series of models, based on a simple geometric abrasion-ablation formalism, was developed and showed reasonable agreement with atmospheric (Wilson et al., 1987) and ground-based measurements (Shavers et al., 1993, Wilson et al., 1991). As development of transport procedures progressed to nucleons and light ions, additional models were needed to describe the broad energy distributions associated with lighter mass particles produced through intra-nuclear collisions and target deexcitation. To fill this gap, parametric representation of Bertini model simulations were utilized (Wilson et al., 1991).

As transport procedures progressed beyond the simple straight-ahead approximation (Clowdsley et al., 2000), it became apparent that the collection of nuclear interaction models used within HZETRN needed improvement to clarify whether

discrepancies against limited space flight data and Monte Carlo simulations were caused by transport approximation or nuclear physics errors. A two-tiered approach was adopted to address this problem. In one tier, specific components of the existing nuclear physics models (i.e. collection of NUCFRG and parametric fits to Bertini and QMSFRG (Cucinotta et al., 2007) results) would be improved. This led to an updated model, referred to as NUCFRG3 (Adamczyk et al., 2012) with corrections for light particle production through electromagnetic dissociation (EMD) interactions (Adamczyk and Norbury, 2011; Adamczyk et al., 2013) and coalescence (PourArsalan and Townsend, 2013). In the other tier, a more fundamental and comprehensive approach would be taken, wherein existing models would be replaced entirely with a self-consistent formalism able to produce necessary interaction parameters for all space relevant particles and energies. This led to a model based on relativistic multiple scattering theory (Werneth and Maung, 2013) able to describe meson production (Werneth and Maung, 2013) and couple with de-excitation models to compute fragmentation cross sections. In both tiers, the primary emphasis was placed on nucleon and light ion production, as these particles dominate exposures behind space relevant shielding (Walker et al., 2013; Norbury and Slaba, 2014) and represent the largest gap in ground-based experimental data and nuclear model uncertainty (Norbury and Miller, 2012; Norbury et al., 2012).

3.1 NUCFRG3 and Electromagnetic Dissociation

In nucleus-nucleus collisions, light ions can be produced in a variety of ways. If the projectile nucleus hits the target nucleus in a head-on or grazing collision, particle production occurs via the strong interaction. If the projectile misses the target, but still passes close by, then the nuclei interact via the electromagnetic (EM) force, which is sufficiently large to also result in particle production through the EMD process. For neutron and light ion production, EMD cross sections can be comparable in size to nuclear interaction cross sections (Norbury and Maung, 2007). Pair production (Norbury, 2006) and electroweak processes (Ahern and Norbury, 2003, 2004) are also possible. Strong interaction production of neutrons and light ions can occur through either direct processes (direct knock-out, pick-up or stripping) or through abrasion-ablation processes, where an excited fragment is formed after a strong nuclear interaction (abrasion), with the fragment subsequently decaying (ablation). A second process for light ion production is through coalescence, in which protons or neutrons produced after ablation can interact with each other, and coalesce into heavier isotopes of hydrogen and helium.

The NUCFRG series of codes describe production of nucleons and ions from nucleus-nucleus collisions through a simple geometric abrasion-ablation model. Details of the model are described elsewhere (Wilson et al., 1994), but of particular interest here are the updates focused on light ion production released with NUCFRG3 (Adamczyk et al., 2012). In NUCFRG3, the previous EMD model (Wilson et al., 1994) was replaced with an improved model based on Weisskopf-Ewing

theory (Adamczyk et al., 2013) able to predict nucleon and light ion production. Comparisons to limited experimental data showed that the updated model was comparable to the older EMD model used in NUCFRG2 for nucleon production, but also represented the additional light ion production channels with reasonable accuracy. Further correction to the light ion production channels was provided by integrating a coalescence model developed by PourArsalan and Townsend (2013).

Following this work, a new electromagnetic dissociation (EMD) model was developed (Norbury, 2013) that provides many significant improvements over the EMD model used in NUCFRG3 (Adamczyk et al., 2012). A new computer code called EMDFRG (Norbury, 2013), can be incorporated into a variety of different transport codes. The model includes single nucleon and light ion production, as well as multiple nucleon production (such as two protons and one neutron in coincidence with an alpha particle) not present in the previous model. Also high linear energy transfer (LET) fragment production is better described. The model has been compared to the complete set of available experimental measurements, and represents the most extensive validation of any EMD model. It also shows much better agreement for the important process of alpha particle production, compared to the older model. Some examples of data comparisons are shown in Figure 9.

3.2 Relativistic Multiple Scattering and De-excitation

Many nuclear models rely on multiple scattering theory (MST) to describe the interaction. Physical observables, including the elastic differential, reaction, elastic, and total cross sections, are found from the scattering amplitude, which may be obtained by solving the Lippmann-Schwinger (LS) equation directly using the three-dimensional Lippmann-Schwinger equation (LS3D), or by using approximate solution methods, such as the partial wave (PW) analysis and Eikonal approaches. Within MST, nucleon-nucleus (and nucleus-nucleus) interactions are modeled as the sum of residual nucleon-nucleon interactions between the projectile and target nuclei. In the non-relativistic theory, the residual interaction can be separated from the unperturbed Hamiltonian, and the transition matrix can be expressed in a multiple scattering series, such that the leading term is the sum of the pseudo two-body transition operator, known as the Watson-tau operator. The goal of MST is to express the Watson-tau operator in terms of the free two-body operator that can be parameterized to nucleon-nucleon experimental data.

Relativistic effects have been included through the development of a relativistic multiple scattering theory (RMST) for nucleus-nucleus scattering (Werneth and Maung, 2013), and by the inclusion of relativistic kinematics in the Lippmann-Schwinger equation. One of the motivations for RMST was to provide a channel through which pions could be produced in the final observed state. Werneth and Maung (2013) developed a relativistic multiple scattering theory (RMST) for nucleus-nucleus scattering that includes the delta resonance in the intermediate state, which can later produce pions through a decay mechanism. The RMST

differs from the non-relativistic MST in that the residual interaction is not readily separated from the Hamiltonian. An equivalent approach was implemented in which Feynman diagrams were used to formulate the multiple scattering series.

Although the RMST formalism for production of delta resonances provides a channel for pion production through decay, it is difficult to perform this calculation in practice. Consequently, Werneth et al. (2013a) extended a thermal model parameterization (Norbury, 2009a, 2011) in which pions are formed from the Boltzmann decay of a hot ensemble of nucleons, known as a fireball. Double-differential cross sections were integrated and normalized to invariant total cross section parameterizations, and the fireball temperature parameterization was estimated from experimental data. It was found that the thermal model better predicts the double differential cross sections than existing models for energies between 0.4 to 2 GeV/n.

Extensive research has been performed on the PW, LS3D, and Eikonal solution methods of the LS equation for space radiation applications (Werneth et al., 2013b, 2014, 2015). Werneth et al. (2013b) developed new finite summation formulas to achieve more efficient partial wave convergence. Additional progress was made by Werneth et al. (2014) where relativistic kinematics were included in the PW and LS3D solution methods, and new numerical methods allowed for computation of the elastic differential cross section at energies much higher than preceding studies. Furthermore, it was shown (Werneth et al., 2015) that there is no observed difference between the elastic differential cross sections for projectile and target nuclei of equal mass in nuclear collisions. As a consequence of this study, it was shown that relativistic kinematic effects depend on both projectile kinetic energy and the mass difference between the projectile and target.

The PW, LS3D, and Eikonal solution methods were validated against a comprehensive database of elastic, reaction, total, and elastic differential cross sections. The models accurately produce cross sections for laboratory projectile kinetic energies greater than 220 MeV/n (Werneth et al., 2017a). As expected, relativistic model results were shown to be in better agreement with data than non-relativistic models. The Eikonal solution method accurately predicts elastic differential cross sections at medium energies, but relativistic PW and LS3D models were shown to make better predictions for higher energies. In a follow-up paper (Werneth et al., 2017b), it was shown that the relativistic LS3D model could predict reaction cross sections with the same fidelity as the Tripathi reaction cross section model (Tripathi et al., 1999), as shown in Figure 10. Moreover, the relativistic LS3D model may be used to compute total, elastic, and elastic differential cross sections as well. It was recommended that the relativistic LS3D model should be used for making predictions of cross sections when limited experimental data are available to validate results, where parametric models are less likely to produce accurate predictions.

The nuclear models developed thus far are well-suited for a relativistic abrasion/ablation model that will be used to describe nuclear fragmentation. An effort is underway to combine the relativistic abrasion model with de-excitation models into a new code known as the Relativistic Abrasion-Ablation De-excitation FRaG-

mentation (RAADFRG) model. Nuclear de-excitation may proceed through the Weisskopf-Ewing formalism, multifragmentation, Fermi-breakup, or other mechanisms. Often, nuclear de-excitation is described by Weisskopf-Ewing decay at lower excitation energies and multifragmentation or Fermi-breakup at higher excitation energies (David, 2015). At high excitation energies, nuclear matter may undergo a phase transition in which the nuclear matter segregates into fragments of intermediate mass compared to the original nucleus (Bondorf et al., 1995). A paper was published (Pshenichonov et al., 2010) using Geant4 with the NUCFRG2-inspired abrasion-ablation model coupled with multifragmentation to examine the effect of multifragmentation on nuclear fragmentation modeling. The paper showed a significant increase in the cross section for fragments with charge Z = 3 - 7, which are sometimes called intermediate mass fragments. This pointed to the need to include multifragmentation in the nuclear physics models used at NASA.

The canonical thermodynamic model (CTM) of multifragmentation (Das et al., 2005) uses the canonical partition function, and characterizes the disintegrating nucleus by temperature, mass, charge, and freeze-out volume. All multifragmentation models use the same physics; that is to say, the fragments are produced according to their statistical weights within the available phase space. The choice of the canonical partition function leads to a simplified set of recursion relations for the partition function and, therefore, the distribution of fragments of a given mass and charge (Botvina et al., 2008). These recursion relations are numerically efficient compared to the Monte Carlo methods used for other statistical multifragmentation models and are ideal for inclusion in the nuclear models used for space radiation analysis.

Initially, CTM was coupled into RAADFRG as part of the de-excitation phase of nuclear fragmentation. After the abrasion step was finished, the excitation energy of the pre-fragment was calculated. If that excitation energy was below 3 MeV/nucleon, the code would de-excite the nucleus through Wiesskopf-Ewing ablation model. If the excitation energy was above 3 MeV/nucleon, then the nucleus would undergo multifragmentation, and the spectra of final products were calculated with the CTM model. The critical excitation energy of 3 MeV/nucleon was chosen because this is the excitation energy where sequential decay of the nucleus is expected to break down (Bondorf et al., 1995). RAADFRG computes excitation energy for the pre-fragment, but CTM requires the temperature for the fragment. Since the conversion from excitation energy to temperature is system dependent, the CTM model was used to calculate caloric curves for all possible pre-fragments through nickel on the periodic table. These caloric curves are used to convert the excitation energy computed from RAADFRG in a self-consistent manner within CTM to nuclear temperature and used as input into the CTM. Additional research and validation is needed to assess the impact of this model for various projectile/target systems. Work continues to improve RAADFRG as a replacement for NUCFRG3 in space radiation analyses, as it is based on a self-consistent relativistic multiple scattering theory and de-excitation framework able to describe nuclear structure effects in an computationally efficient manner.

3.3 Experimental Data Mining and Gaps

Heavy ion fragmentation produces a spectrum of charged fragments with energy and direction very near that of the incident projectile ion, while the lightest fragments and nucleons tend to have broader energy and angle distributions, especially if target de-excitation contributions are considered. Nucleon induced collisions result in a quasi-elastic peak of nucleons produced in the forward direction with a broadly dispersed component at lower energies associated with intra-nuclear collisions and target de-excitation/evaporation.

These separations in phase space between forward-directed projectile-like fragments and dispersed target-like fragments are a critical feature of the perturbative solutions implemented in HZETRN. It also requires different types of cross section data depending on the type of interaction being considered. For space applications, the heavy ions produced from nucleus-nucleus collisions may be accurately treated within the straight-ahead and velocity conserving approximations (Wilson et al., 2006), thereby requiring only total fragmentation cross sections to be used in transport solutions. Light ions and nucleons, on the other hand, are produced at broad energies and angles, therefore requiring single and/or double differential cross sections in the transport procedures. Experimental data collection for nuclear model validation followed this same separation.

To address heavy ion nuclear model uncertainty, total fragmentation cross section data (i.e. integrated over outgoing particle energy and angle) are needed. Experimental heavy ion fragmentation data from the open literature were assembled, and a database was created which consists of over 3,600 cross sections with 25 distinct projectile isotopes from ^{10}B to ^{58}Ni, a projectile kinetic energy range of 90 MeV/nucleon to 14.5 GeV/nucleon, and both elemental and compound targets ranging from hydrogen to uranium (Norman and Blattnig, 2013). The experimental data were taken from 30 different publications which described experiments performed at eight different facilities around the world, including the Joint Institute for Nuclear Research in Dubna, Russia, the Heavy Ion Medical Accelerator in Chiba, Japan, and the Super Proton Synchrotron at CERN near Geneva, Switzerland.

Neutron and light ion production data needs to be in the form of double-differential cross sections as a function of both energy and angle because neutrons and light ions are produced at a variety of energies and a variety of angles. A comprehensive review of all of the available cross section data for all ions (light, medium, and heavy) was undertaken, and its relevance to space radiation applications was thoroughly discussed (Norbury and Miller, 2012; Norbury et al., 2012). The most important finding of these studies was that the biggest gap in cross section measurement data are light ion production double-differential cross sections.

A database, called NUCDAT, was produced that includes more than 50,000 entries to nuclear reaction experiments of relevance to space radiation studies. These include references to all types of cross sections including total, single and double-differential and Lorentz invariant differential. The database is searchable over reaction particles, year, author, etc. Results from this database have been put in

graphical form (Norbury and Miller, 2012; Norbury et al., 2012), and an example is shown in Figure 11, where the symbol (D) represents where double-differential cross section measurements have been performed. The example shows ^{4}He fragment production measurements, at a variety of energies. Only two measurements have been made in the energy range 3 - 15 GeV/n, and there are no measurements above 15 GeV/n. There are no measurements for Fe projectiles.

A set of recommendations was made with priorities for nuclear cross section measurements most suitable for testing space radiation nuclear cross section models and transport codes. The highest priority recommendations were listed in Tables 5 and 6 of Norbury et al. (2012). The highest priority measurements were identified as He fragments, with the next highest priority being H fragments.

3.4 Uncertainty Quantification

To assess the applicability of nuclear models to space radiation shielding applications, systematic verification, validation, and uncertainty quantification procedures were implemented. Direct comparison between theoretical results and experimental data is needed, but this is not always possible due to the paucity of experimental data. For space radiation applications, the cross section data should represent the GCR environment with an energy spectrum from 10 MeV/n - 1 TeV/n and a projectile mass distribution from hydrogen to nickel. In addition, the experimental database should contain data from targets commonly used in spacecraft shielding, and information on all possible fragments produced from a given projectile-target combination is important. This is a vast phase space to cover for validation purposes.

Uncertainty quantification in applications where experimental data are sparse required special consideration in order to arrive at meaningful results. Norman and Blattnig (2013) developed uncertainty metrics specifically for nuclear model validation which included experimental error and focused on addressing questions of model consistency and accuracy with experimental values. The overall effort found that NUCFRG2 (Wilson et al., 1994) and QMSFRG (Cucinotta et al., 2007) were equivalent with regard to global accuracy compared to the experimental data.

In addition, areas of model improvement for NUCFRG2 were identified and include improved energy dependence and nuclear matter description to rectify the increasing uncertainty with larger energy and target mass. Improved descriptions for ΔZ=1 and ΔZ=2 reactions, where ΔZ is the charge difference between the beam and the measured fragment, are also needed. Measurements of charge-changing and fragmentation cross sections were made by Zeitlin et al. (2008a, 2008b, 2010, 2011) and compared with a variety of nuclear physics models. Figure 12 shows nuclear fragmentation model cross sections compared to experiment for the ^{40}Ar + C reaction with a projectile energy of 610 MeV/n. While NUCFRGG2 agrees well with most of the data, it is unable to account for the peak observed for carbon (fragment charge Z = 6), whereas the peak does appear in the PHITS model, although it is

under-predicted. The correct description of this peak in nuclear models is thought to be related to multifragmentation, discussed in the prior section. Figure 13 shows model uncertainties for the fragmentation of ^{14}N, ^{16}O, ^{20}Ne, and ^{24}Mg between 290 and 1000 MeV/n on a variety of targets. A model with an uncertainty of less than 0.25 is considered very accurate, while values above 1.0 are quite inaccurate.

4 Radiation Transport

The deterministic transport code, HZETRN, was originally developed by Wilson et al. (1991) as a means of investigating GCR exposure levels and protection requirements for NASA. At that time, computational resources were limited, and Monte Carlo methods were therefore constrained in their ability to inform such studies. The guiding approach adopted for HZETRN was to develop a converging sequence of physical approximations from simple to increasingly complex, with methods to evaluate the code against design and operational requirements along the way. Highly efficient, yet physically simple, tools could therefore be applied early in the design cycle and mission planning stages when shielding architectures and other requirements are not precisely defined. More complex and accurate tools would be applied later in the design optimization process to verify against fully realized requirements. Within this paradigm, efficient one-dimensional solutions based on the straight-ahead approximation were developed first. Corrections to the 1-dimensional (1D) codes were then systematically applied until a complete 3-dimensional (3D) solution was developed and connected to detailed and realistic spacecraft mass geometry.

4.1 One dimensional transport

In ∼2005, Wilson et al. (2006) described the historical context for early stages of HZETRN development and provided an overview of the code at that time as well as future directions. HZETRN2005 was entirely based on the one-dimensional (1D) straight-ahead approximation, with coupled numerical solutions for light particles ($Z \leq 2$) and heavy ions ($Z > 2$). In about the same time, the NASA Standard for Modeling and Simulation (NASA, 2006) was being formulated, which communicated an increased focus on verification, validation, and uncertainty quantification for models used by NASA. Versions of HZETRN were also being selected for web-applications such as SIREST (Singleterry et al., 2001), OLTARIS (Singleterry et al., 2011) and CREME (Tylka et al., 1997). Given the increased scrutiny on model development practices, systematic efforts were undertaken to bring HZETRN in line with NASA standards and provide a more suitable software for the various applications being considered.

Since HZETRN is a deterministic code, relevant energy and spatial variables must be discretized onto pre-defined grids over which solutions are evaluated with numerical methods. Importantly, the code does not rely on finite differencing, finite

element, or differential equation solvers (Wilson et al., 1991), but still utilizes various methods for interpolation and integration that carry some degree of numerical error. Quantifying and controlling these numerical errors are critical components of code verification as outlined in the NASA standard (NASA, 2006).

Slaba et al. (2010c) conducted energy grid convergence studies to quantify accuracy of some of the numerical methods used in the code. The study showed that prior versions of HZETRN were inadequately treating neutron elastic interactions within non-hydrogenous targets were energy transfers are exceedingly small, leading to unpredictably large numerical errors for shielding levels beyond $\sim$20 g/cm^2. Methods were developed to address the problem, which resulted in a multigroup-like approximation being implemented. This correction greatly reduced numerical error and provided a robust solution over a wide range of energy grid configurations.

A follow-on study (Slaba et al., 2010a) then examined coupled convergence of energy grid and physical step-size. Charged particles lose energy due to atomic interactions as they propagate over a given spatial step-size. This is reflected in HZETRN solution methodologies which are based on the method of characteristics (Wilson et al., 1991). In practical terms, this implies that numerical errors in deterministic solutions are simultaneously influence by fidelity in the energy grid and spatial step-size. The study of Slaba et al. (2010a) quantified the step-size and energy grid requirements needed to reach converged solutions. Additional sensitivity tests revealed the need for double precision arithmetic (single precision had been historically used). Most importantly though, new numerical methods were introduced for light particle transport that reduced run-times by a factor of 100 for SPE boundary conditions and a factor of 10 for GCR boundary conditions.

Further work (Slaba et al., 2013c) provided a perturbative approach allowing converged solutions to be obtained ($<$3% numerical error) with computationally efficient step-sizes and energy grids. A final technical report introduced a method for further reducing GCR analysis run-times by a factor of $\sim$2 without altering numerical error (Slaba et al., 2013d). These combined studies provided a highly efficient and robust set of numerical methods that turned out to be essential in the development of more sophisticated transport formalisms.

Having settled the underlying numerical methods used for 1D neutron and ion transport, attention was shifted to pion and muon transport methods previously developed specifically for HZETRN (Blattnig et al., 2004). Aghara et al. (2009) used the MCNPX Monte Carlo simulation code to investigate pion contributions to exposure levels behind shielding. It was found that pions account for 20% or more of the dose behind shielding. A fine, but important, detail was that pion contributions to dose in this study included both direct (i.e. direct energy deposition by charged pions) and indirect (i.e. secondary particles produced through pion decay or pion-induced nuclear collisions) components. The direct pion contribution to dose is $\sim$10% or less in most deep space shielding scenarios, while the indirect pion contribution can be quite significant. Neutral pion decay, in particular, results in the production of two energetic photons with the ability to initiate an EM cascade.

At about this same time, Nealy et al. (2010) had been developing deterministic photon, electron, and positron transport methods for efficient analysis of environmental conditions near Jovian moons. These deterministic methods included the dominant EM interactions (i.e. bremsstrahlung, pair production, annihilation, and inelastic processes) for space applications that would connect easily to existing pion and muon codes. The combination of HZETRN with deterministic muon/pion transport and coupled EM transport was described by Norman et al. (2012, 2013). Comparison against atmospheric measurements (Norman et al., 2012, 2013), ISS data (Slaba et al., 2013a) and recent comparisons to MSLRAD data (Matthia et al., 2016, 2017) suggest the model is reasonably accurate, as shown in Figure 14.

However, coupling of the pion field to the nucleon field was neglected. In atmospheric cascades, pions are more likely to decay before initiating a nuclear event, and therefore, the importance of the pion nuclear coupling term is not obvious. In bulk shielding on the other hand, charged pion nuclear interaction path lengths are shorter than decay lengths, and therefore, pions contribute moderately to the nucleon field below a few hundred MeV. A fully coupled pion/nucleon transport model is now being developed to address this problem.

4.2 Bi-directional transport

The straight-ahead approximation is highly accurate in describing heavy ion transport. However, neutrons and light ions are produced over a broad momentum distribution, necessitating a more detailed theoretical formalism. Clowdsley et al. (2000) began investigating improvements to the straight-ahead approximation for low energy (<400 MeV) neutron transport. These early methods separated neutron production into forward and isotropic components. The forward component, associated with projectile-like fragments and nucleon-induced quasi-elastic secondaries, was accurately treated within the straight-ahead approximation. While the isotropic component could be further separated into forward and backward terms, thereby providing a first perturbation away from simple 1D solutions. Notably, the forward and backward transport solutions were not coupled, so that the multiple elastic collisions which dominate low energy neutron transport were not fully described.

To address this point, Slaba et al. (2010b) developed a rapid Neumann series solution that fully accounts for all of the elastic collisions at low energies. This code was compared to fully three dimensional Monte Carlo simulation codes in slab geometry (Slaba et al., 2010b; Heinbockel et al., 2011a, 2011b), lunar surface configurations (Slaba et al., 2011b) and on the surface of Mars (Matthia et al., 2016, 2017). In general, it was found that the HZETRN bi-directional neutron transport agreed with the Monte Carlo codes to the extent they agree with each other. Despite the improvements, the bi-directional methods have noticeable limitations in finite geometry, where particle leakage through off-axis, or lateral, boundaries can be significant. This may be particularly important in vehicle and habitat mass geometries that are not well-approximated by simple slabs or spheres.

4.3 Three dimensional transport

The next natural step in transport code development focused on 3D methods. Wilson et al. (2014) described an initial 3D model (3DHZETRN), wherein the isotropic component of the neutron production was coupled to finite geometry and treated along discrete angular directions. Whereas the prior bi-directional model only considered forward and backward transport (relative to the incoming boundary condition direction), the first 3D model considered a set of angular directions covering the full 4π steradian over which the neutron production term would be evaluated. Convergence tests showed that relatively few angular directions (less than 20) were needed to achieve a stable solution for space applications, especially when the incoming boundary conditions are applied isotropically over the entire shielding mass.

Comparisons with Monte Carlo simulation codes showed significant improvement in describing low energy neutron and light ion spectra. These comparative studies considered a range of shielding geometries, including slabs with finite and infinite lateral dimensions (Wilson et al., 2014, 2015a; Slaba et al., 2017), spheres with one material (Wilson et al., 2014), spheres with two materials (Wilson et al., 2015b), and combinatorial geometry with multiple spheres and boxes contained within a closed cylinder (Wilson et al., 2016). Methods were also developed to connect the 3DHZETRN to existing engineering and risk analysis computational frameworks wherein vehicle geometries are described using CAD software in full detail (Slaba et al., 2016a).

Figure 15 shows a comparison between 3DHZETRN and Monte Carlo simulations in combinatorial geometry. Values labeled as 3DHZETRN (N=1) correspond to a 1D solution, while values labeled as 3DHZETRN (N=26) correspond to a converged 3D solution. The improvements offered by the 3D methods are clear and are in good agreement with the Monte Carlo results. It is also worth noting that the 3DHZETRN results ran in $\sim$60 seconds on a desktop computer, while the Monte Carlo codes required $\sim 10^8$ CPU seconds (spread over a cluster).

Although these efforts were a significant step forward for NASA's radiation transport code, limitations of the forward/isotropic formalism carried into the 3D solution were discovered. It was found that estimates of neutron lateral leakage contained some error due to inadequate treatment of low energy diffusive processes (Wilson et al., 2015a). Rapid transition in the low energy light ion flux occurring within microns of material interfaces (e.g. aluminum-to-water) were also not being fully captured, since only the neutrons were being evaluated in 3D (Wilson et al., 2014).

To address these issues, Wilson et al. (2017) provided a further extension to the transport formalism where in the forward/isotropic assumption was removed, and light ions were fully included in the 3D solution. This allowed the full angular dependence of neutron and light ion production expressed through the double differential cross sections to be considered (instead of just approximating the angular dependence with an assumed isotropic distribution). Figure 16 shows a comparison between the updated version of 3DHZETRN and Geant4 simulations near a material interface. In this plot, the fluences are multiplied by LET to highlight the low

energy region. It has been previously shown (Wilson et al., 2006) that the product of fluence and LET approaches a constant value for charged particles at low energies. However, when secondary ions are produced in one material near an interface and leak into the adjacent material, a rapid transition occurs in the low energy spectrum as a result of material dependencies in the LET values. The important point of this comparison is that the updated 3DHZETRN code accurately captures this highly detailed rapid transition in the low energy proton flux near the interface between two distinct materials.

The extension of deterministic transport procedures in HZETRN to 3D has allowed a clear distinction to be drawn between nuclear physics model uncertainty and transport method uncertainty. In past comparisons between deterministic and Monte Carlo solutions (Heinbockel et al., 2011a,b; Slaba et al., 2010b; Norbury et al., 2017), interpretation of spectral differences were clouded by the use of differing nuclear physics models and deterministic methods that relied on the straight-ahead or bi-directional approximations. These new 3D deterministic transport solutions appear highly accurate in the range of geometry and boundary condition scenarios considered, suggesting that any observed differences between deterministic and Monte Carlo codes are mainly a result of nuclear model differences. The generation of a nuclear physics model database from a Monte Carlo code for direct inclusion in 3DHZETRN would confirm this hypothesis and is the focus of current work. Current efforts in transport code development are focused on including the EM, muon, and pion components into the 3D formalism while maintaining computational efficiency. Of particular note is the coupling between the pion and nucleon fields, which can be significant in moderately thick mass shielding.

The most recent version of the transport code, HZETRN2015, is available at https://software.nasa.gov. The code comes with transport model options (1D, bi-directional, or 3D) in slab, combinatorial, or ray-trace geometries. In other words, HZETRN2015 includes 1DHZETRN, 2DHZETRN, or 3DHZETRN as options. Boundary condition environments can be selected or defined by the user, and various output quantities are automatically evaluated.

5 Highlighted Applications

The previous sections describe collective efforts to improve models and understanding of the space radiation environment, nuclear physics, and particle transport. Results from these efforts are disseminated through publications, but more importantly, through a variety of applications or capabilities that were previously unavailable. In this section, some of the end-products that rely on or utilize the models described in this paper are discussed. Though not described in detail here, other web-based platforms that utilize versions of HZETRN include EMMREM (http://emmrem.unh.edu) and PREDICCS (http://prediccs.sr.unh.edu). The NASA cancer risk model (Cucinotta et al., 2013) also uses HZETRN to determine the radiation field quantities needed for risk projection. This section is also intended

to represent applications of the work discussed in the previous sections. These specific applications are chosen because they represent some of the most important advances in space radiation physics and transport. Even though there may be a small amount of overlap with previous sections, these applications are highlighted for ease of reading, especially for the wider biology and space management communities that may be more interested in seeing how all the various environment, transport and nuclear physics models of the previous sections actually get used to advance space radiation protection.

5.1 OLTARIS

The On-Line Tool for the Assessment of Radiation in Space (OLTARIS) (Singleterry et al., 2011), brings the various radiation models and analysis methods described in the previous sections (as well as other international models) together in a convenient tool available to the world-wide space radiation shielding community. OLTARIS is a website that maintains a set of best-practices in models and methods that allows engineers and scientists to run complete radiation analyses without the need of being an expert in the various codes and models being evaluated.

After registering at the site and gaining access, the user is presented with simple-to-use forms guiding them through the setup of a radiation analysis. This includes the selection of an external environment or boundary condition (SPE, GCR, LEO, Lunar and Mars surface), selection or definition of a shielding geometry (multi-material, multilayer spheres, slabs, ray-traced thickness distributions), and finally, selection of the desired output quantities (dose, whole-body effective dose, fluence spectra, etc.). Once the analysis details, or project, is defined, the user can send a job for processing. An email is sent to the user when the job is complete, so that results can be viewed or downloaded.

The OLTARIS website is based on the most up-to-date version of the HZETRN code with the associated nuclear physics models (Adamczyk et al., 2012). Additionally, fully detailed human phantom models that have been adapted for space applications (Slaba et al., 2010d) may be selected by the user.

The framework for the site is modular so that new models and methods can be added as they become available. All software is version controlled, and the users are given tagged version numbers in their results to ensure repeatability and traceability of results. A changelog is maintained on the site so that users know when new models or methods are added, and when exiting models have been updated. The original site was deployed in 2008, and supported a basic set of models and responses. Since that time, more than 65 updates have been made, deemed important enough to include in the changelog. A complete list of capabilities and tools can be found on the homepage located at https://oltaris.nasa.gov. The OLTARIS website currently has roughly 600 active accounts and averages 8000 analysis runs per year.

5.2 NAIRAS

There is a recognized need to link scientific knowledge of atmospheric cosmic radiation impacts to aviation decision making with respect to aircrew and passenger exposure (Fisher, 2009). Commercial aircrews are classified as radiation workers by the ICRP (ICRP, 1991). This designation is accepted by most countries, including the United States of America (USA), Canada and the European Union (NCRP, 2009; Lindborg et al., 2004). The NCRP found that crews of commercial aircraft received the largest effective dose compared to other terrestrial radiation workers monitored during the same study period (NCRP, 2009). Nevertheless, USA aircrews represent an occupational group exposed to undocumented and unquantified radiation levels over the duration of their careers. In addition, the current ICRP guidelines for maximum prenatal and public exposures can be exceeded during a single solar storm event for passengers on cross-polar or intercontinental commercial routes, or by frequent use ($\sim$5-10 round-trip flights per year) of these high-latitude routes even during quiet solar conditions, in the absence of SPE events (AMS, 2007, Copeland et al., 2008; Dyer et al., 2009; Mertens et al., 2012).

A significant step forward in quantifying and documenting aircraft radiation exposure has been made via the development of NASA's Nowcast of Atmospheric Ionizing Radiation for Aviation Safety (NAIRAS) model. NAIRAS is the first real-time, global, physics-based aviation radiation model which includes both GCR and SPE sources of atmospheric cosmic radiation (Mertens et al., 2012, 2013). It also incorporates the dynamical response of the geomagnetic field to variations in the interplanetary medium (Kress et al., 2010; Mertens et al., 2010). NAIRAS real-time graphical and tabular products are streaming live from the public web site at http://sol.spacenvironment.net/$\sim$nairas/. An example of the real-time products is shown in Figure 17 for the January 2012 solar storm event.

The NAIRAS model provides data-driven, global, real-time predictions of atmospheric ionizing radiation exposure rates on a geographic 1×1 degree latitude and longitude grid from the surface of the Earth to 90 km with a vertical resolution of 1 km. The real-time, global predictions are updated every hour. Physics-based models, including a version of HZETRN, are utilized within NAIRAS to transport cosmic rays through three distinct material media: the heliosphere, Earth's magnetosphere, and the neutral atmosphere. The physics-based models are input-driven by real-time measurement data, which are used to: (1) specify the ionizing radiation field at the boundaries of the aforementioned material media, and (2) characterize the internal properties of the aforementioned material media. The real-time measurements provide necessary observational constraints on the physics-based models that improve simulations of the transport and transmutations of cosmic radiation through the heliosphere, magnetosphere, and atmosphere. More details of the salient features of the NAIRAS physics-based radiation environment and transport models are described by Mertens et al. (2010, 2012, 2013).

The NAIRAS model predictions of GCR atmospheric radiation dose rates were compared with reference measurement data tabulated in a joint report of the Inter-

national Commission on Radiation Units and Measurements (ICRU) and the ICRP (ICRU, 2010), and also compared to onboard aircraft radiation measurements taken in 2008 (Mertens et al., 2013). The NAIRAS/ICRU comparisons of ambient dose equivalent rate were generally within +50% for any single-point comparison, and generally within 25% at cutoff rigidities less than 4 GV (or, latitudes poleward of 30-degrees). Radiation measurements taken by the German Aerospace Center (DLR) in 2008 on a high-latitude and a low-latitude flight during the minimum between solar cycle 23 and solar cycle 24 were also analyzed. The two DLR flight measurements covered the range of geomagnetic cutoff rigidities at commercial aircraft flight levels. The comparison of NAIRAS to TEPC (Tissue Equivalent Proportional Counter) ambient dose equivalent rates were generally within 10% for the high-latitude flight, and roughly within 50% for the low-latitude flight.

The ICRU criterion on acceptable uncertainty in dose assessment of aircraft ionizing radiation exposure at commercial flight levels is that the combined relative standard uncertainty should not exceed 30% for an assessment of ambient dose equivalent equal to or greater than an annual dose of 1 mSv. When this criterion is applied to the combined NAIRAS/ICRU and NAIRAS/DLR comparisons, the differences are within ±25%. Therefore, based on the ICRU/ICRP criterion, the NAIRAS model can be reliably used in commercial aircraft radiation risk assessment and radiation mitigation decisions for GCR exposure.

Due to limited availability and accessibility to aircraft radiation measurements during solar-geomagnetic storms, NAIRAS model predictions of SPE atmospheric radiation exposure have not yet been validated. Continuous aircraft radiation measurements on select high-latitude flights would quickly close the measurement data gap that is prohibiting the development and validation of accurate and reliable aircraft radiation model predictions during radiation and geomagnetic storms, which is an activity currently being pursued (Tobiska et al., 2015; Straume et al., 2016).

The NAIRAS model has been recently updated to use the 2015 version of HZETRN (Slaba et al., 2016a; Wilson et al., 2016), which includes the pion-initiated electromagnetic cascade processes. A preliminary reassessment of the ICRU reference measurement data and the DLR aircraft measurements described above have shown a significant improvement in the NAIRAS model predictions, especially for low-latitude (high-cutoff rigidity) absorbed dose quantities. Moreover, the RaD-X flight campaign has provided an unprecedented set of dosimetric measurements at the same geomagnetic cutoff rigidity, which includes seven altitudes from commercial flight levels to above the Pfotzer maximum where the dosimetric quantities are influenced by cosmic ray primaries (Mertens et al., 2016a, 2016b). Extensive comparisons between the new version of NAIRAS (version 2.0) and these measurement datasets are the subject of ongoing research activities.

5.3 GCR simulator at the NASA Space Radiation Laboratory (NSRL)

The GCR environment consists of protons and heavier ions spanning the periodic table of elements with energies ranging from tens of MeV up to the TeV region. To address uncertainties in biological responses to this type of radiation exposure, experiments are performed at ground based facilities such as the NASA Space Radiation Laboratory (NSRL). Due to facility and other practical constraints, most of the experiments performed to date have utilized single ion mono-energetic beams over short durations to irradiate animals and cells, which has always been known to be a poor representation of the actual space radiation environment. Though this approach was mainly a result of facility constraints, significant knowledge was gained regarding the mechanisms through which particle radiation damages cells and tissue and either induces or promotes various biological outcomes. Biophysical models were also developed to interpret and combine the available mono-energetic, single ion acute experimental data into usable tools for risk projection (Cucinotta et al., 2013).

NSRL is now able to reliably switch ions and energies in very short time scales ($\sim$1 minute), suggesting a practical capability to simulate the GCR environment on the ground. To begin developing a ground based GCR simulation capability, an international collaboration was formed which focused on describing current and possible future issues associated with such experiments (Norbury et al., 2016). A comprehensive study was also completed to identify the deep space radiation environment that would be simulated (Slaba et al., 2016b). The study was made possible by the efficiency of HZETRN, which allowed multiple complex vehicle and habitat shielding configurations to be analyzed at various times in the solar cycle.

GCR simulator experiments will be conducted at NSRL over short and long durations and should help reduce uncertainties associated with radiation quality and dose rate. Moreover, this technology allows robust development and evaluation of biological countermeasures which may reduce the absolute risk levels in spite of existing uncertainties. Future work in the area of GCR simulator development may focus on the combination of shielded (Kim et al., 2015) and unshielded (Slaba et al., 2016b) approaches to enable a practical method for simulating the charged particles and secondary neutrons present in space.

5.4 Minimum in dose equivalent versus depth

Perhaps the most dramatic and unusual new result found in the last decade in space radiation physics and transport research is the appearance of a minimum in the dose equivalent versus depth curve (Slaba et al., 2013a). Typically, one might expect that the radiation dose received would decrease as the amount of shielding is increased. This is seen in Figure 18, which shows both dose equivalent and effective dose decreasing as a function of shield thickness, where an external GCR

environment is incident on the front of a planar shield, with the target point (where dose is calculated) at the back of the shield. The plots in Figure 18 are obtained using HZETRN with straight-ahead transport and no pion contributions.

However, realistic spacecraft shield configurations are more complicated than simple planar shields. In a small capsule, for example, one has an isotropic GCR environment impinging on the outside of the capsule. This GCR environment not only passes through the outside wall, but secondary particles inside the capsule can traverse to the far back wall and undergo further interactions resulting in "albedo" particles coming from the back wall. This "forward-backward" (two-dimensional) transport is more complicated than straight-ahead transport and there are also more complicated three-dimensional effects present all over the capsule. Such a geometry might deviate from the naive expectation of decreasing dose with increasing thickness, because the far walls themselves are extra sources of radiation that come back into the interior of the spacecraft. Similar three-dimensional complications can also be envisaged if the target point is located deep in an astronaut's body, where the whole three-dimensional structure around the target point can contribute to produced radiation.

In order to investigate the effects discussed above, a simplified shielding geometry is shown in Figure 19, which illustrates the forward-backward contributions from front and back shields to a target point located in the middle. The GCR particles are incident from the left, as indicated by the arrow. Calculations have been performed with this configurations and in the following discussion it is important to be clear as to how shielding thickness is now defined. A thickness of x g/cm^2 will now mean x g/cm^2 for the front shield, as well as x g/cm^2 for the back shield. The tissue thickness is always 30 cm.

Calculated results for both aluminum and polyethylene are shown in Figure 20 using the straight ahead[2] approximation, bi-directional neutron solution[3], and 3D solution[4] described in section 4.3. The straight-ahead results show the similar dose equivalent with increasing depth seen previously. The bi-directional solution shows a local minimum, but at a larger thickness ($\sim$40 g/cm^2) than what is predicted by HZETRN2015 and the Monte Carlo codes. The HZETRN2015 result includes 3D scattering for neutrons and light ions and appears to be in reasonable agreement with the ensemble of Monte Carlo codes. The unexpected increase of dose equivalent beyond the local minimum near 20 g/cm^2 is primarily due to the build-up of secondary neutrons produced in the front and back shields. These neutrons produce high LET fragments with short range that contribute significantly to dose equivalent. Although not shown, it has been verified that at very large thicknesses beyond 100 g/cm^2, the dose equivalent again falls monotonically with increasing shield thickness. Both the dose equivalent curves for polyethylene, and the effective dose curves for aluminum and polyethylene do not show an increase at large depths

[2]Labeled HZETRN2005.
[3]Labeled HZETRN2010.
[4]Labeled HZETRN2015.

due to the absorption of neutrons by hydrogen in polyethylene and tissue.

The occurrence of a minimum in the dose equivalent versus depth curve changes the spacecraft radiation shielding paradigm. Previously, it was thought that more shielding results in better radiation protection. However, these new findings show that increased aluminum shielding beyond the minimum at 20 g/cm^2 actually results in worse radiation protection, and adding a hydrogen rich shielding material, such as polyethylene or human tissue, beyond 20 g/cm^2 has a only very small impact on astronaut exposure. These results lead to a new spacecraft design paradigm in which minimum mass designs are sought which utilize onboard systems and stowage to ensure at least 20 g/cm^2 of shielding surround astronauts in as many locations as possible, and effort is not expended to provide larger quantities of shielding.

5.5 Pion contribution to dose

The contributions of pion production to space radiation dose (not dose equivalent) has been investigated in several papers (Aghara et al., 2009; Norman et al., 2012; Slaba et al., 2013b) using cross section parameterizations (Norbury 2009a, 2009b, 2009c, 2011; Werneth et al., 2013a). An essential aspect of these parameterizations was that they clearly showed that the use of a thermal model for pion production was far superior to previously developed models. This is shown in Figure 21, where the thermal model is able to reproduce experimental cross section data much better than previous models.

The pion contribution to dose was first investigated by Aghara et al. (2009), where it was shown that the pion contribution could be as large as 20% in 30 g/cm^2 tissue, as shown in Figure 22. In this figure, the pion contribution consists of both the pion and photon contributions, because photons are a result of pion decay. Further results for pion contribution to dose is shown in Figure 23 using a full GCR spectrum. It can be seen that the pion contribution to dose can be as large as 40% for very thick shielding.

The large contribution of pions to dose for thick shielding regions represents another significant and important new discovery in space radiation physics. Previously it was postulated that pions could be somewhat important. The surprising new result is that pion contributions to dose can be so large, and thus the effects of pion production, and the associated electromagnetic cascade (EMC), must be included in space radiation transport codes.

The effect on dose equivalent will be much smaller due to the relatively small quality factor of pions. However, the full quality factor effect of negative pions, which can induce nuclear spallation processes, where the entire nucleus "explodes" due to the presence of a negative pion, is larger and may need further investigation. The unusual reaction mechanisms of negative pions led to the investigation of negative pion therapy for cancer treatment (Petti and Lennox, 1994).

5.6 Neutron and light ion contribution to dose equivalent

For many years, space radiation investigators have been performing space radiobiology experiments at the NASA Space Radiation Laboratory (NSRL) and elsewhere, with a very typical setup being the use of Fe and other heavy beams, typically at the relatively high energy of 1 GeV/n. With the more widespread availability of lighter beams with a variety of energies, it is important to determine which beams are the most important for space radiation applications. It has been pointed out (Norbury and Slaba, 2014) that heavy nuclei contribute significantly to dose equivalent only for thin shielding, such as 5 g/cm^2, whereas for the typical thicker shielding of about 20 g/cm^2 used in modern spacecraft, the contribution of Fe to dose equivalent is small, because heavy nuclei get broken up into smaller secondary fragments as they traverse thick shielding. This is illustrated in Figure 24, where, it can be seen that for many detector locations, it is the neutrons and light ions that dominate dose equivalent (Walker et al., 2013). In several detector locations the contribution of heavy ions is almost negligible. It is also interesting to analyze these contributions as a function of energy. Due to slowing down of GCR particles in shielding, the relevant contributions as a function of energy are significantly lower than 1 GeV/n (Slaba et al., 2016a).

The large contribution of lower energy neutrons and light ions (and the small contribution of high energy heavy ions) to dose equivalent for realistic shielding thickness is an important result. The old paradigm of performing radiobiology experiments using beams of Fe at 1 GeV/n means that one is investigating the effects of an ion that produces essentially negligible contribution to dose equivalent and effective dose, although these experiments are useful for understanding the biological mechanisms and effects of high LET radiation. (A caveat is that if there are thinly shielded regions of a spacecraft, then the effects of heavy ions can be important.) The overall conclusion is that neutron and light ion experiments are just as important as heavy ion investigations.

5.7 Comparison of American (NASA) and Russian (ROSCOSMOS) space radiation tools

A program comparing space radiation calculations between the American (NASA) and Russian (ROSCOSMOS) space agencies has recently begun. Several workshops in Moscow have been held, with radiation experts sharing calculations and results from a wide variety of space radiation topics. The activity has recently included other space agencies from Europe, Japan, and Canada. Three papers resulting from this work have already been published (Norbury et al., 2017, 2018a, 2018b). These studies are discussed below.

5.7.1 Transport codes

The first direct comparisons of the American (NASA) and Russian (ROSCOSMOS) space radiation transport codes, HZETRN, and SHIELD have recently been preformed (Norbury et al., 2017). Flux spectra of neutrons, light ions, heavy ions, and pions were calculated for galactic cosmic ray H, O, and Fe projectiles incident on an Al cylinder of varying thickness. Comparisons of Geant4 and FLUKA transport codes were also shown, and comparisons between HZETRN and SHIELD included a comparison of pion flux. HZETRN, SHIELD, and FLUKA were found to be in excellent agreement for thick (100 g/cm^2) shielding for H, O, and Fe projectiles, and also in excellent agreement for high energy (>500 MeV) pion production from H projectiles for thinner (1, 10 g/cm^2) shielding. However, for thinner (1, 10 g/cm^2) shielding, poor agreement with HZETRN was obtained for O and Fe projectiles, and for lower energy (<500 MeV) pion production from H projectiles, with HZETRN results significantly smaller than SHIELD and FLUKA. These differences for thinner shielding were thought to be due to differences in nuclear models which are expected to manifest themselves for thin shields.

5.7.2 Pion cross sections

The thin shield issues mentioned above were further investigated by comparing nuclear models directly (Norbury et al., 2018b). The question was why HZETRN gave consistently smaller results than SHIELD for transport through targets of varying thickness. The aim was to investigate whether differences seen were because of smaller cross sections or differences in transport methods. It was found that differences in the pion nuclear cross sections were significant enough to account for the differences in the transport codes, and it was concluded that further cross section model improvements were necessary.

5.7.3 Galactic cosmic ray models

The third paper in the NASA versus ROSCOSMOS comparison series involves GCR models (Norbury et al., 2018a), which are compared with recent measurements of cosmic ray Hydrogen, Helium, and the Boron-to-Carbon ratio from the Alpha Magnetic Spectrometer (AMS). One of the major insights is that the new AMS data (Aguilar et al., 2015a, 2015b, 2016) has sufficiently good statistics to clearly distinguish between the various model predictions, which included the NASA GCR Badhwar-O'Neill model (O'Neill et al., 2015), the ROSCOSMOS International Standardization Organization (ISO) GCR model (Nymmik et al., 1992, 1994, 1996; ISO, 2004), the new SINP (Skobeltsyn Institute of Nuclear Physics) model (Kuznetsov et al., 2017), and also the European Space Agency DLR (Deutsches zentrum für Luft- und Raumfahrt) model (Matthiä et al., 2013).

6 Summary

Characterization of the space radiation environment for missions in LEO, deep space, or near planetary surfaces will require accurate and efficient models with a wide range of applicability. The current set of tools developed and improved over the past decade or so appear reasonably accurate in this regard, although areas requiring further research and development still exist and should be resolved.

Current models used to describe the GCR environment in deep space (Matthia et al., 2013; O'Neill et al., 2015) are highly accurate for retrospective analyses in which heliospheric conditions may be described by known indices such as neutron monitor count rate or sunspot number. Projecting future solar activity has been examined by others (Pesnell, 2012) but remains challenging and highly uncertain. Future mission planning is still made possible by comparing back to historical extrema, for which models provide suitable information. Further refinements to the currently available GCR models should be expected as the AMS-II (Aguilar et al., 2018) and PAMELA (Martucci et al., 2018) instruments have provided high fidelity measurements of the proton and helium spectra over critical energies at monthly time points covering multiple years. Such data will be invaluable to model validation and calibration and should be examined in detail. Leveraging these science instruments to obtain data of interest to astronaut radiation protection should continue.

Nuclear physics models used in radiation transport codes are widely varying in their theoretical formulation and range of applicability. For space radiation analysis, the range of energies, particle types, and interaction types often requires transport codes to combine or blend a variety of nuclear physics models that collectively satisfy the requirements to perform needed calculations. Ground based measurements of pertinent nuclear physics quantities have been summarized by Norbury et al. (2012) and show distinct gaps for particle types and energy regions of interest to space radiation protection. Inter-code comparisons (Heinbockel et al., 2011a,b; Norbury et al., 2017; Slaba et al., 2017) and validation against limited space flight spectral data (Slaba et al., 2011a, 2013a; Matthia et al., 2016, 2017) also highlight moderate to large uncertainties in certain cases. Continued research and development in the area of nuclear physics should continue in order to close the remaining gaps. Particular emphasis should be given to the area of neutron and light ion production from heavy ion fragmentation and nucleon induced target fragmentation. The current lack of relevant data would preclude any model developments or improvements from being objectively evaluated. As such, a complementary program of highly focused ground based experimental measurements is needed.

Transport code development efforts at NASA have provided the HZETRN model, which has made significant contributions to space radiation protection, as outlined in the manuscript. Recent progress in transport model development has successfully extended the 1D formalism to an angular dependent 3D formalism for neutrons and light ions. Additional work is needed (and ongoing) to fully couple the pion interactions to nucleon production and extend the electromagnetic processes to a

suitable level of 3D description. Finally, given the diversity of nuclear physics models available in current transport codes and lack of experimental data to objectively identify the optimal nuclear interaction package, it would be highly informative to generate a complete interaction database from a single Monte Carlo code and couple the database with HZETRN. In this way, transport model uncertainty can be definitively separated from nuclear physics model uncertainty and differences observed against space flight measurements and inter-code comparisons can be clarified. Work in this area is ongoing as well.

Selected applications and highlights are now summarized.

1. Minimum in dose equivalent versus depth

   One of the most dramatic new results from this project is the appearance of a minimum in the dose equivalent versus depth curve. This is one of the most important discoveries in space radiation physics in the last decade and drastically changes the spacecraft radiation shielding paradigm. Previously, it was thought that more shielding results in better radiation protection. However, the newly discovered minimum shows that increased shielding beyond the minimum actually results in worse radiation protection. Further, there is an optimal thickness (approximately 20 g/cm^2) for the best radiation protection, which significantly alters the way spacecraft need to be designed in order to achieve maximum radiation protection.

2. Pion contribution to dose

   The new cross section models and transport methods developed in this project have enabled quantitative estimates of pion contribution to dose in space radiation environments. It has been found hat the total pion contribution (direct and indirect) can be as large as 20% in standard shielding scenarios, and as large as 40% for thick shielding. The large contribution of pions to dose for thick shielding regions represents a significant and important new discovery in space radiation physics.

3. Neutron and light ion contribution to dose equivalent

   For many years, space radiation investigators have been performing radiobiology experiments at the NASA Space Radiation Laboratory (NSRL) and elsewhere, with a common setup being the use of iron and other heavy beams, typically at high energy of 1 GeV/n. With the more widespread availability of lighter beams with a variety of energies, it is important to ask the question as to which beams are the most important for space radiation applications. Calculations performed in this project show that neutrons and light ions dominate dose equivalent for typical spacecraft shielding scenarios, and the contributions from heavy ions at high energy are quite small, except for thinly shielded regions of spacecraft. This is another very important result. The old paradigm of performing radiobiology experiments with high energy heavy ions needs to be significantly expanded to include neutrons and light ions at moderate energies.

4. Measurements

   The large contribution of neutrons and light ions to dose equivalent means that it is important to have nuclear cross section data for these particles in order to validate the nuclear reaction models, which are used as input to transport codes. An extensive evaluation of the available data has been performed under this project and it has been found that the biggest gaps are precisely for the most important particles - neutrons and light ions! Recommendations for future measurements have been made.

5. Three-dimensional transport

   The large contribution of neutrons and light ions to dose equivalent means that transport codes must properly account for these particles. For many years HZETRN has used the one-dimensional approximation. This is a good approximation for high energy heavy ions, but is a poor approximation for neutrons, light ions and pions which in many instances are produced and scattered at large angles, requiring three-dimensional transport methods. Major new developments in three-dimensional transport methods have been made in this project, culminating in the development of a three-dimensional transport code called 3DHZETRN.

6. Relativistic nuclear model

   Surprisingly, many nuclear models used in radiation transport codes do not include the effects of relativity. GCR particles have speeds approaching the speed of light, a regime where relativistic effects become important. A fully relativistic multiple scattering theory has been developed for use in nuclear models for transport codes.

7. GCR simulation

   The galactic cosmic radiation consists of protons and heavier nuclei with energies relevant to space radiation protection from 10 MeV/n to about 50 GeV/n. However, most radiobiology experiments have used single beams at fixed energy. With recent advances in beam switching technology, it is now feasible to rapidly switch ion species and energy, making it possible to simulate the GCR environment with a variety of beams at a variety of energies. A new GCR simulation capability at the NASA Space Radiation Laboratory has been designed within this project. The availability of a GCR simulation capability at NSRL will provide a major new experimental tool for the study of space radiobiological effects.

Finally, Figure 20 also provides a visual summary of the progress made in nuclear physics and transport code development as well as the work still needing to be completed. The various Monte Carlo results share a common transport methodology and differ only in the choice and collection of nuclear physics packages. It can be seen that the HZETRN2005 solution, which relied on the straight-ahead approximation and lacked the pion, muon, and EM components, significantly under-estimates

exposure levels in both aluminum and polyethylene. The HZETRN2010 results provide some improvement as a result of the bi-directional neutron solution, but still lacked the pion, muon, and EM components. Interestingly, this early model shows the local minimum in aluminum near $\sim$40 g/cm^2, and is driven mainly by neutron build-up effects seen in thick shields. The HZETRN2015 includes the pion, muon, and EM components and a 3D solution for neutrons (with partial 3D treatment for light ions) and falls in the range of expected Monte Carlo simulation results in both materials. Substantial progress has clearly been made over the past decade or so, and as highlighted throughout this manuscript, continued research and development is still needed.

Acknowledgments This work was supported by the Human Research Program (HRP) and the Advanced Exploration Systems (AES) Division under the Human Exploration and Operations Mission Directorate of NASA.

	<250 MeV/n	250-500 MeV/n	500-1500 MeV/n	1500-4000 MeV/n	>4000 MeV/n	Total
$Z = 1$	1.2	5.4	18.2	18.4	14.8	58.1
$Z = 2$	1.2	2.2	4.1	2.9	1.7	12.2
$Z = 3$-10	0.0	3.3	3.8	1.3	0.8	9.1
$Z = 11$-20	0.0	0.2	6.6	2.0	1.1	10.0
$Z = 21$-28	0.0	0.0	4.7	3.8	2.1	10.6
Totals	2.5	11.1	37.4	28.4	20.5	100.0

Table 1: Relative contribution ($\times 100$) of GCR boundary energy and charge groups to effective dose with 20 g/cm^2 aluminum shielding. A value of 0.0 indicates that the relative contribution is less than 0.1%.

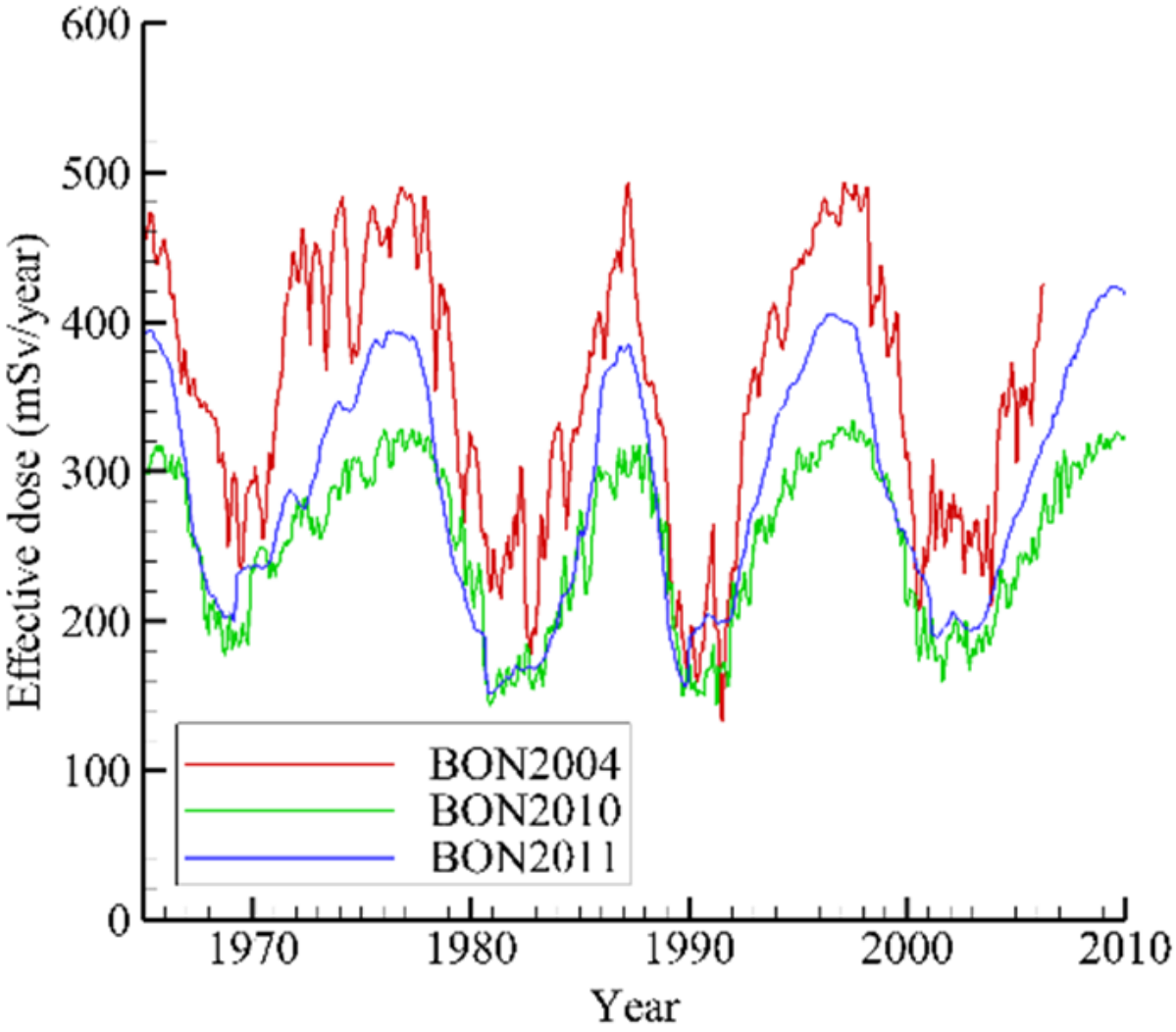

Figure 1: Effective dose (mSv/year) as a function of time for a female astronaut behind 20 g/cm^2 aluminum shielding using three different versions of the BON model for the GCR boundary condition. Reprinted from Slaba and Blattnig (2014a).

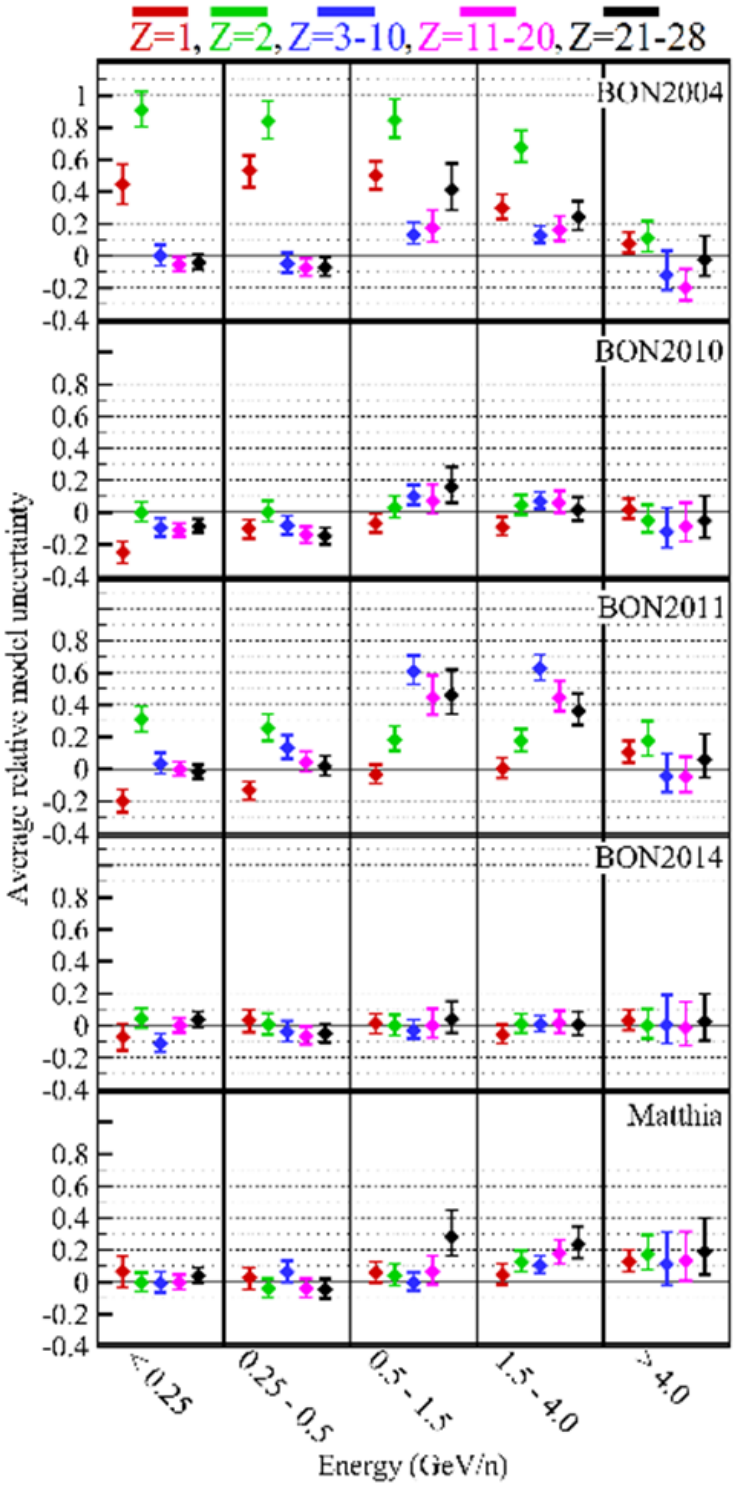

Figure 2: Average model relative uncertainty as a function of charge group and kinetic energy.

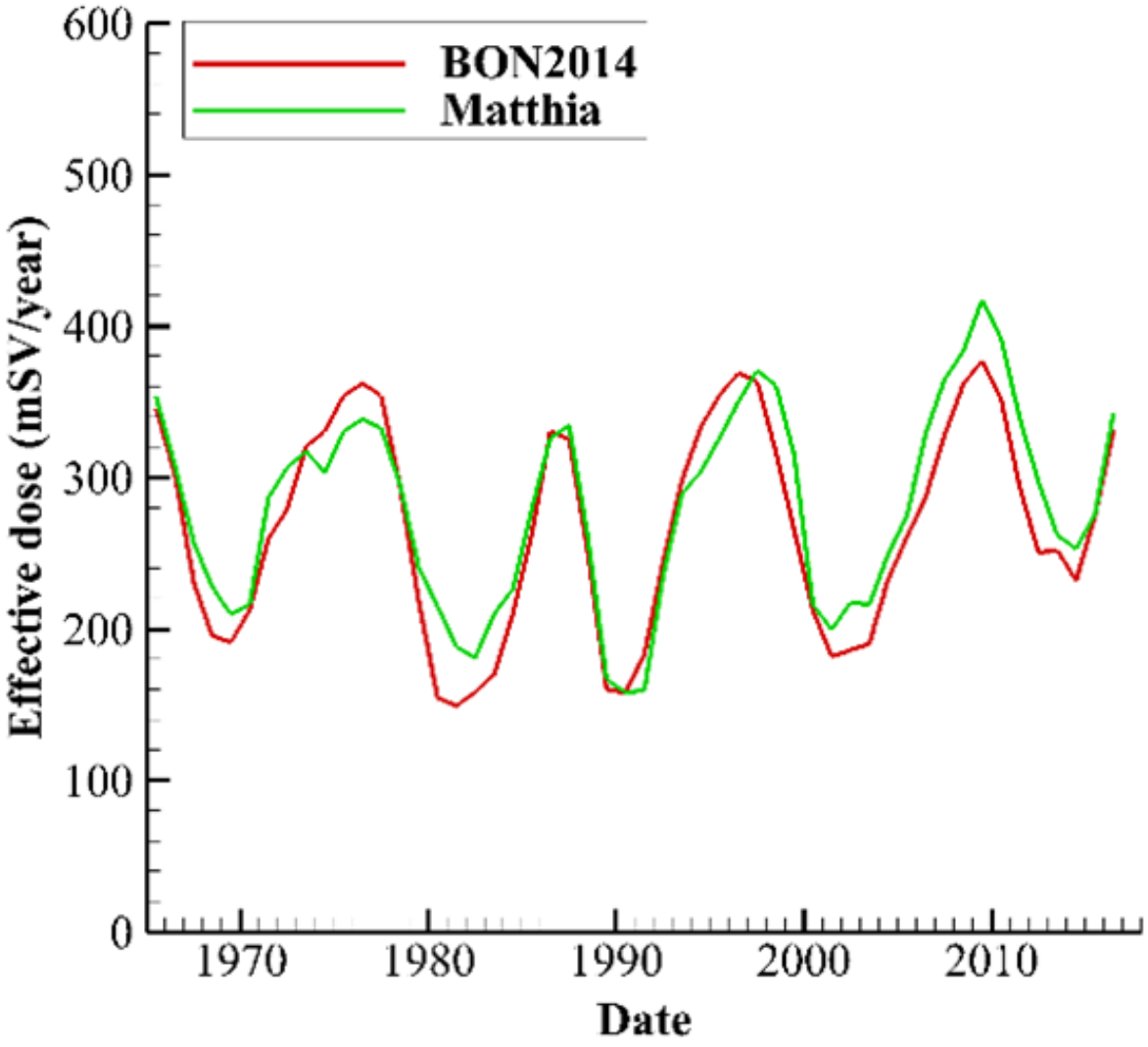

Figure 3: Effective dose (mSv/year) as a function of time for a female astronaut behind 20 g/cm^2 aluminum shielding using updated GCR models.

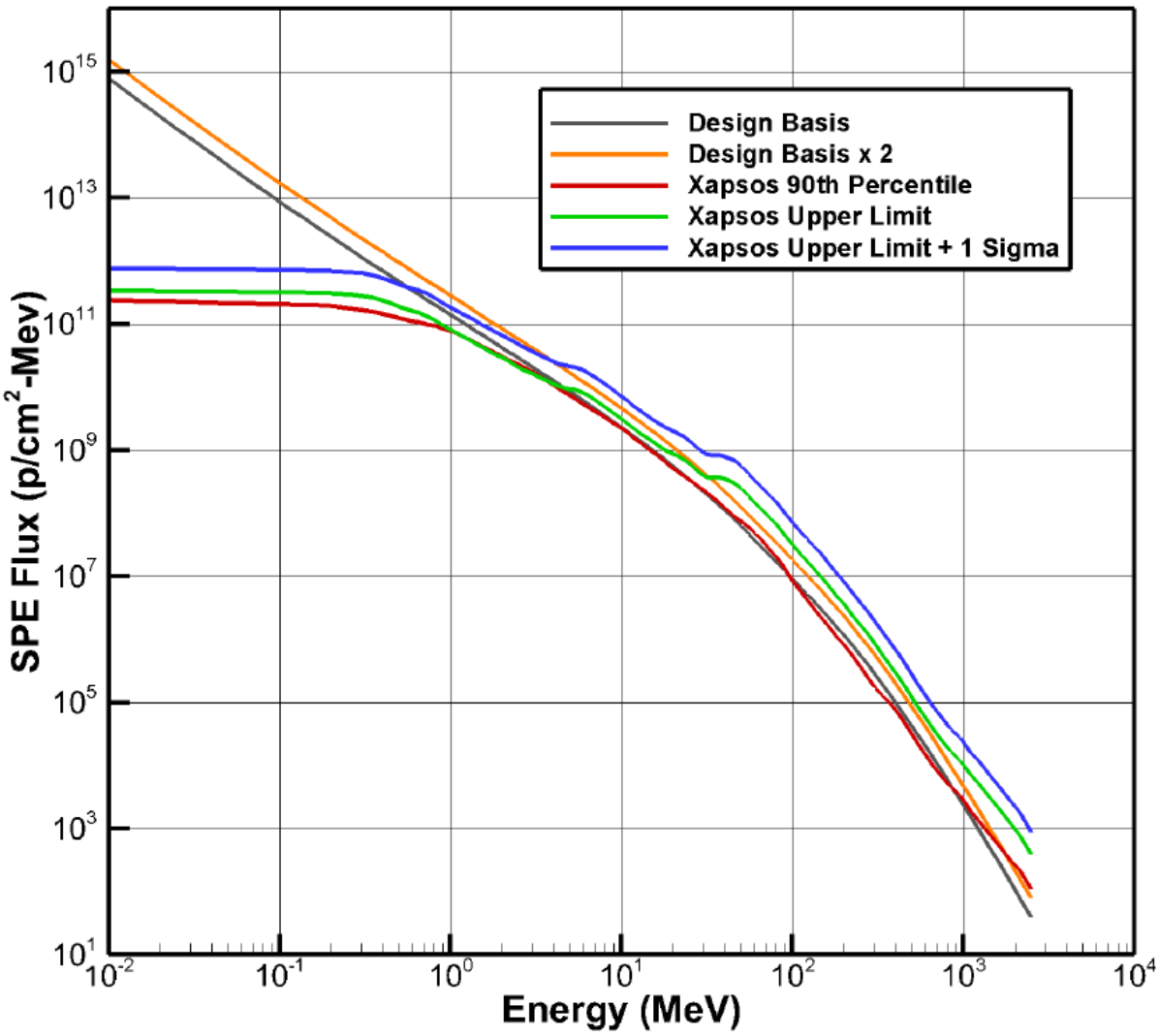

Figure 4: Recommended design reference SPE environment compared to probabilistic model results. Reprinted from (Townsend et al., 2018).

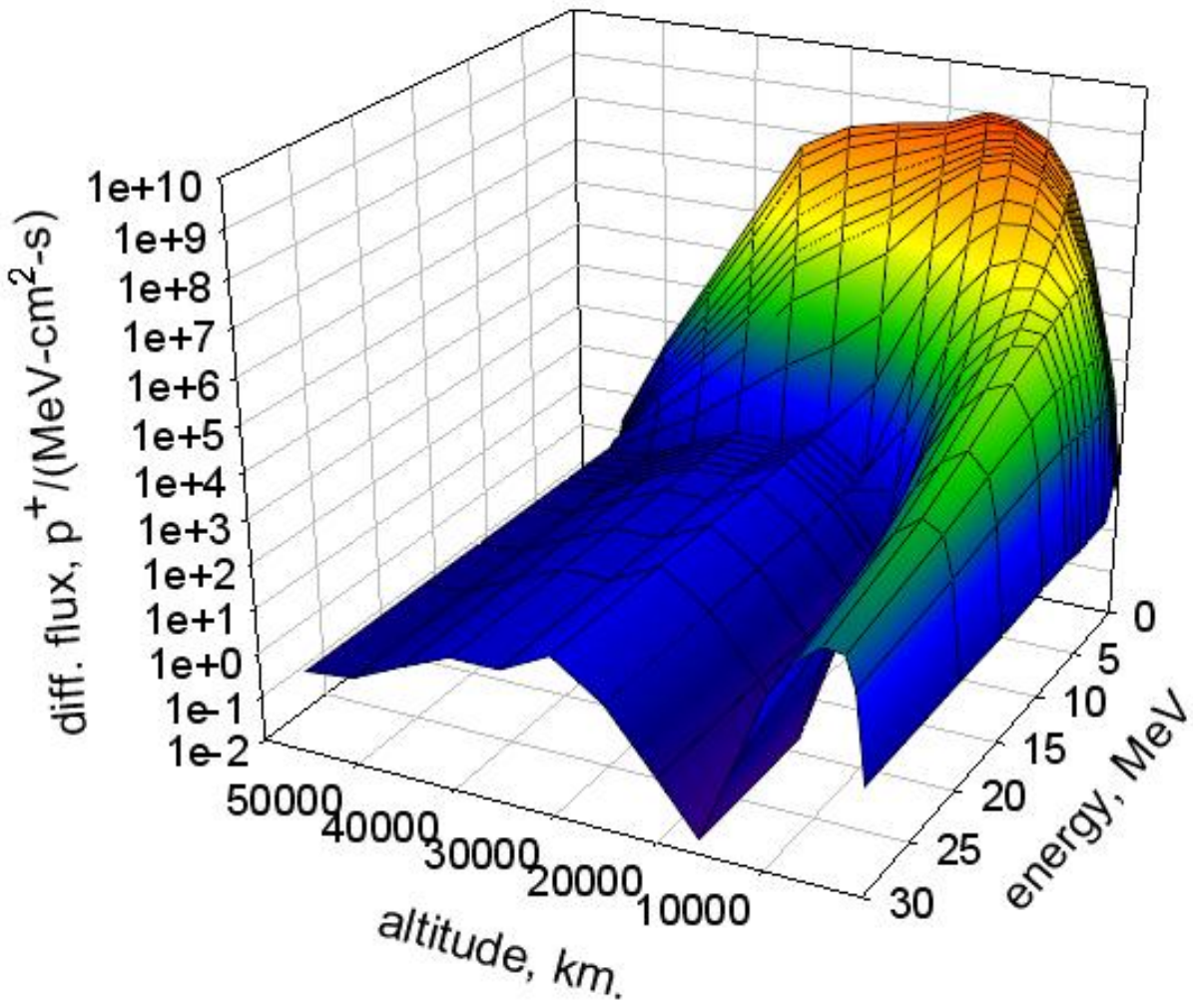

Figure 5: Trapped proton flux and void zones at the equatorial plane. Reprinted from (Badavi et al., 2013).

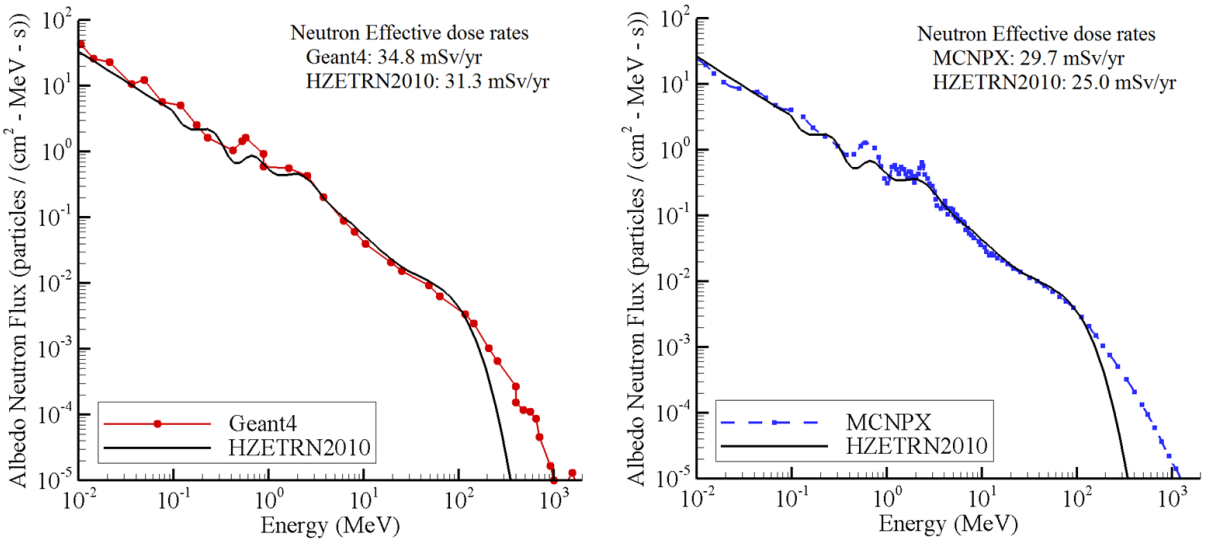

(a) (b)

Figure 6: Comparison of albedo neutron flux generated by various transport codes for two GCR environments approximated with only protons and alphas. (a) 1998/1999 GCR spectrum from (Adams et al., 2007). (b) 1972 GCR spectrum from McKinney et al. (2006). Reprinted from Slaba et al. (2011b).

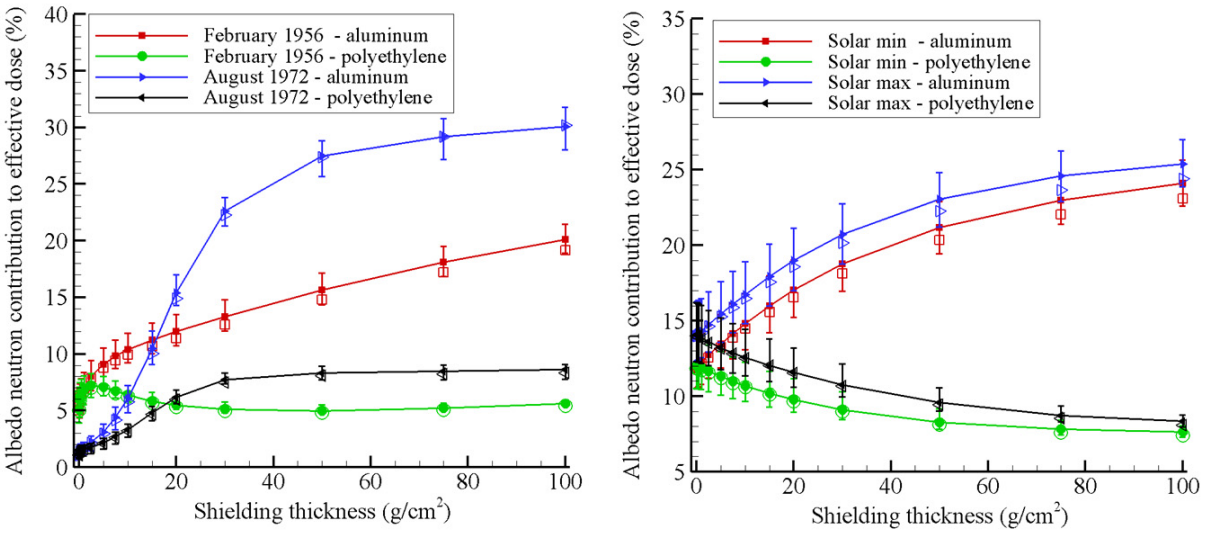

(a) (b)

Figure 7: Albedo neutron contribution to effective dose on the lunar surface in aluminum and polyethylene shielding exposed to (a) SPE and (b) GCR environments. The error bars represent the minimum and maximum results obtained when the neutron component of effective dose was computed with various fluence-to-effective dose conversion coefficients. Non-visible error bars are smaller than the symbols. Closed symbols represent the average result, and open symbols represent the nominal results with HZETRN2010 and ICRP 103 (ICRP, 2007) quality factors and weights. Reprinted from Slaba et al. (2011b).

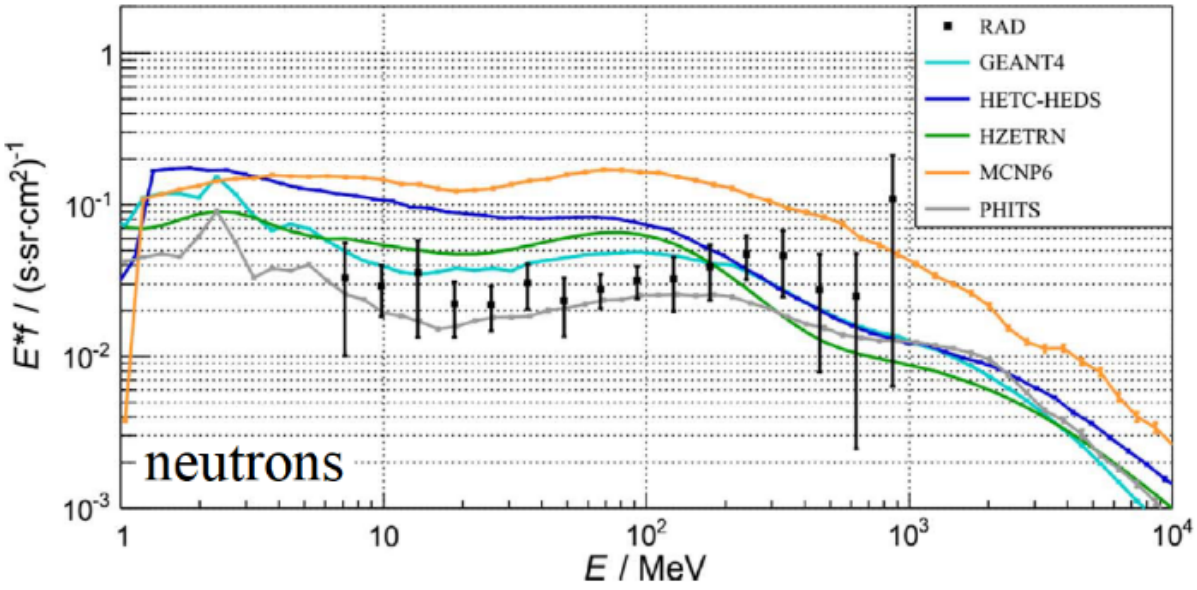

(a)

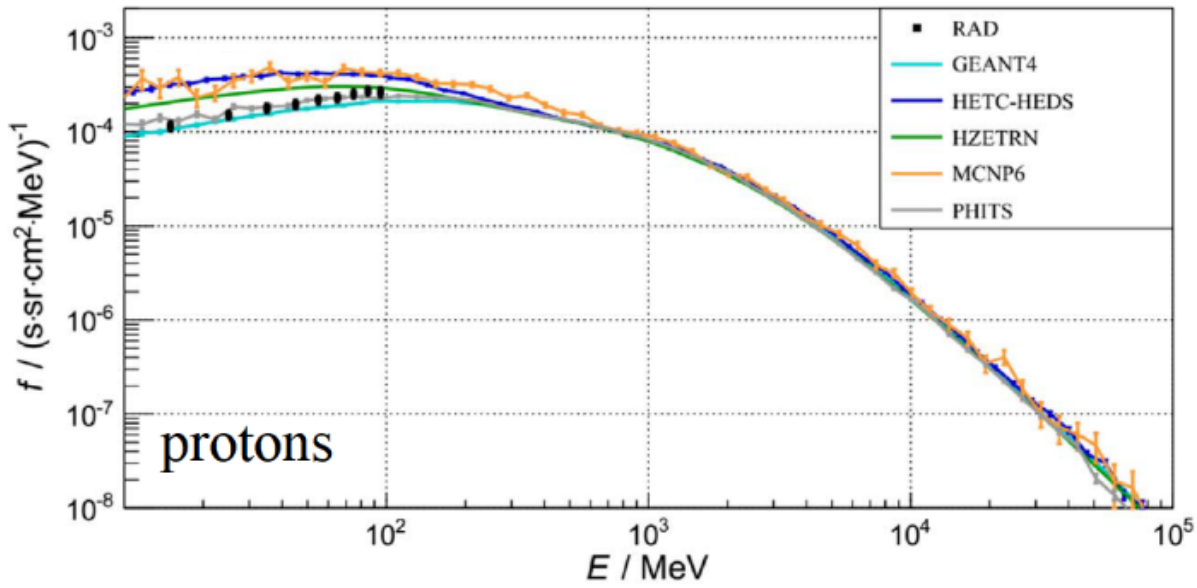

(b)

Figure 8: Comparison of (a) neutron and (b) proton flux estimates from various transport codes to MSLRAD measurements. The neutron flux values have been scaled with energy to reduce the dynamic range of the plot. Reprinted from Matthia et al. (2016).

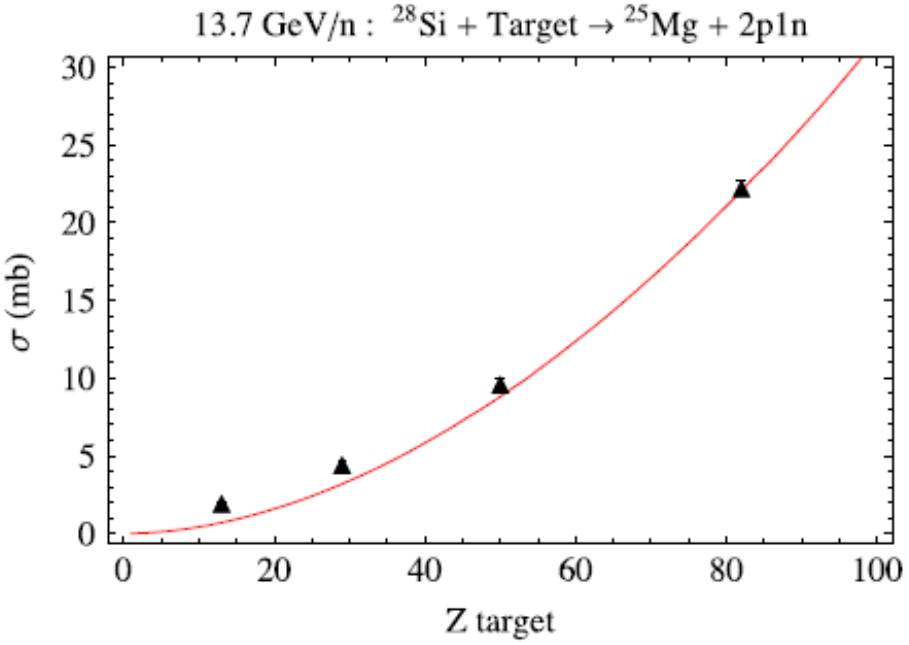

(a)

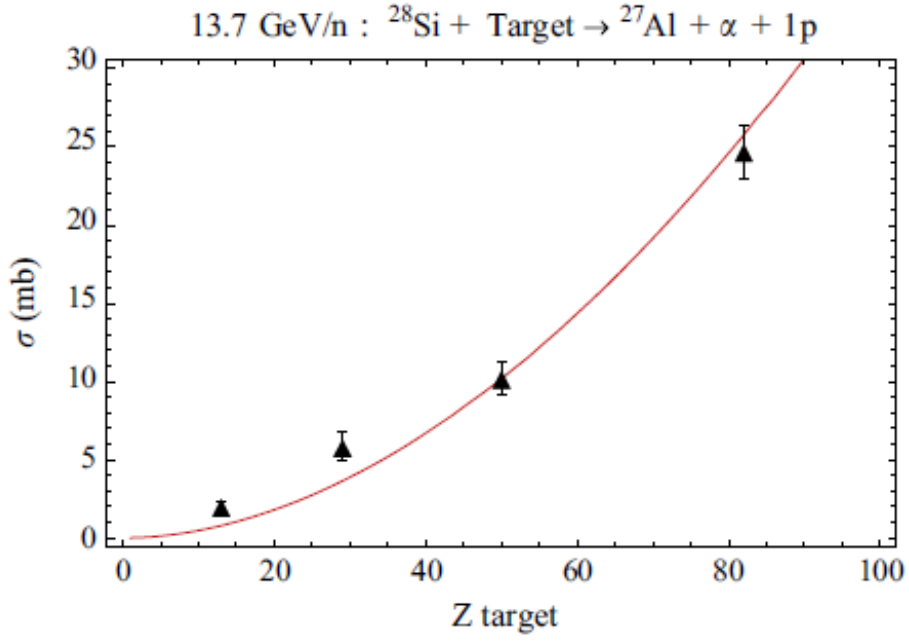

(b)

Figure 9: EMD calculation (red line) versus data (black symbols) for (a) multiple nucleon (two protons, one neutron) removal and (b) one alpha particle and one proton removal at 13.6 GeV/n as a function of target charge. Reprinted from Norbury (2013).

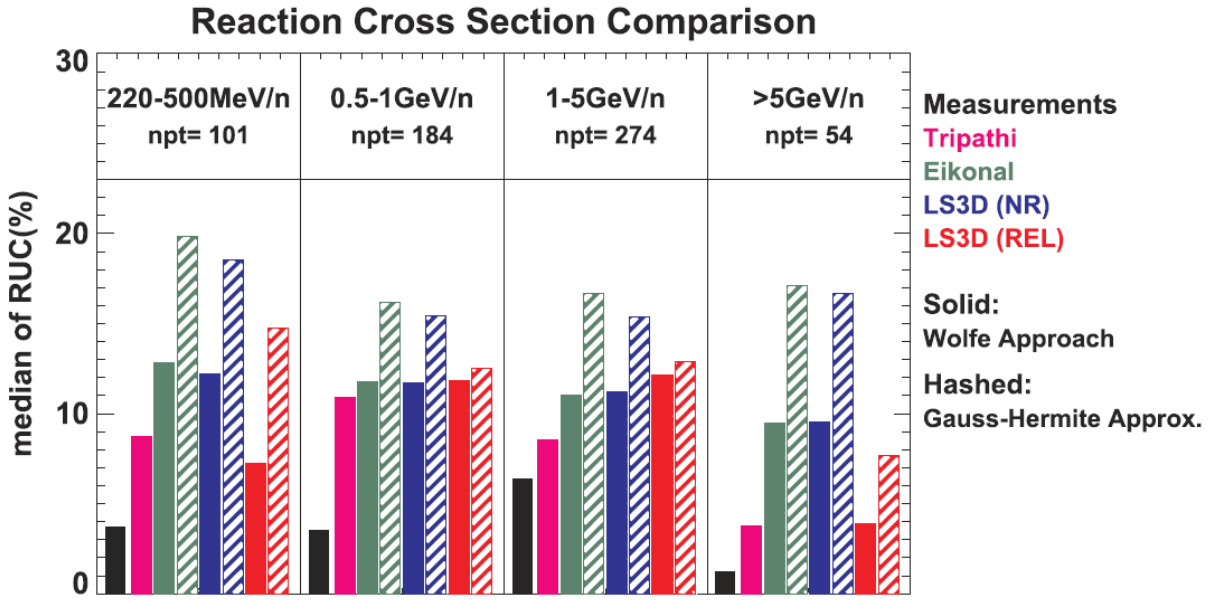

Figure 10: Comparisons of reaction cross section models based on the Eikonal, Lipmann-Schwinger (LS3D) non-relativistic (NR) and relativistic (REL), and Tripathi formalisms. Reprinted from Werneth et al. (2017b).

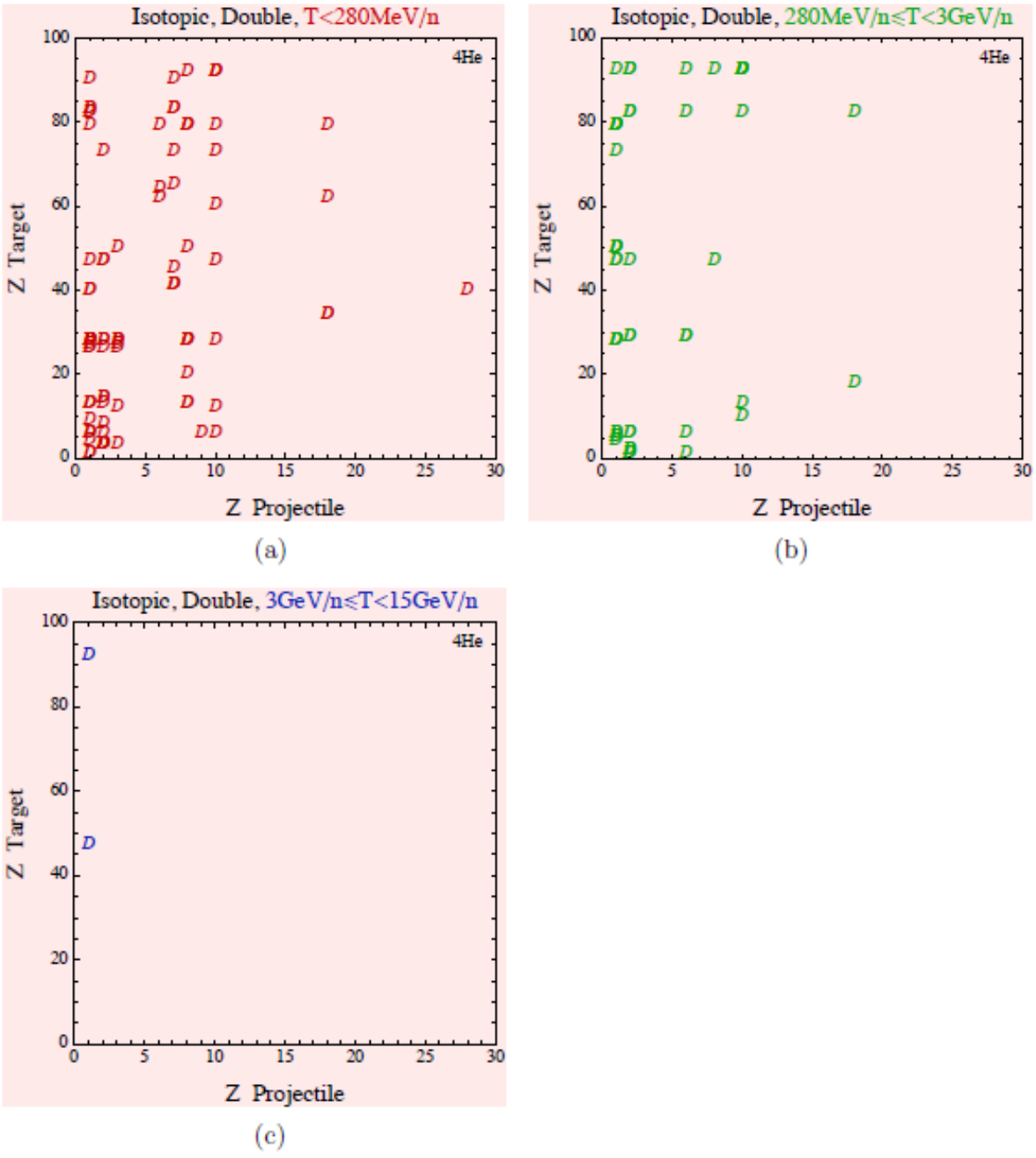

Figure 11: Available isotopic double-differential cross section measurements for ^{4}He fragment production. The symbols D represent where a measurement has occurred. Projectile kinetic energies, T, are listed at the top of each panel. (a) T $<$ 280 MeV/n, (b) 280 MeV/n $\leq$ T $<$ 3 GeV/n, (c) 3 GeV/n $\leq$ T $<$ 15 GeV/n. No measurements are available above 15 GeV/n, which is why the bottom right panel is blank. Reprinted from Norbury et al. (2012).

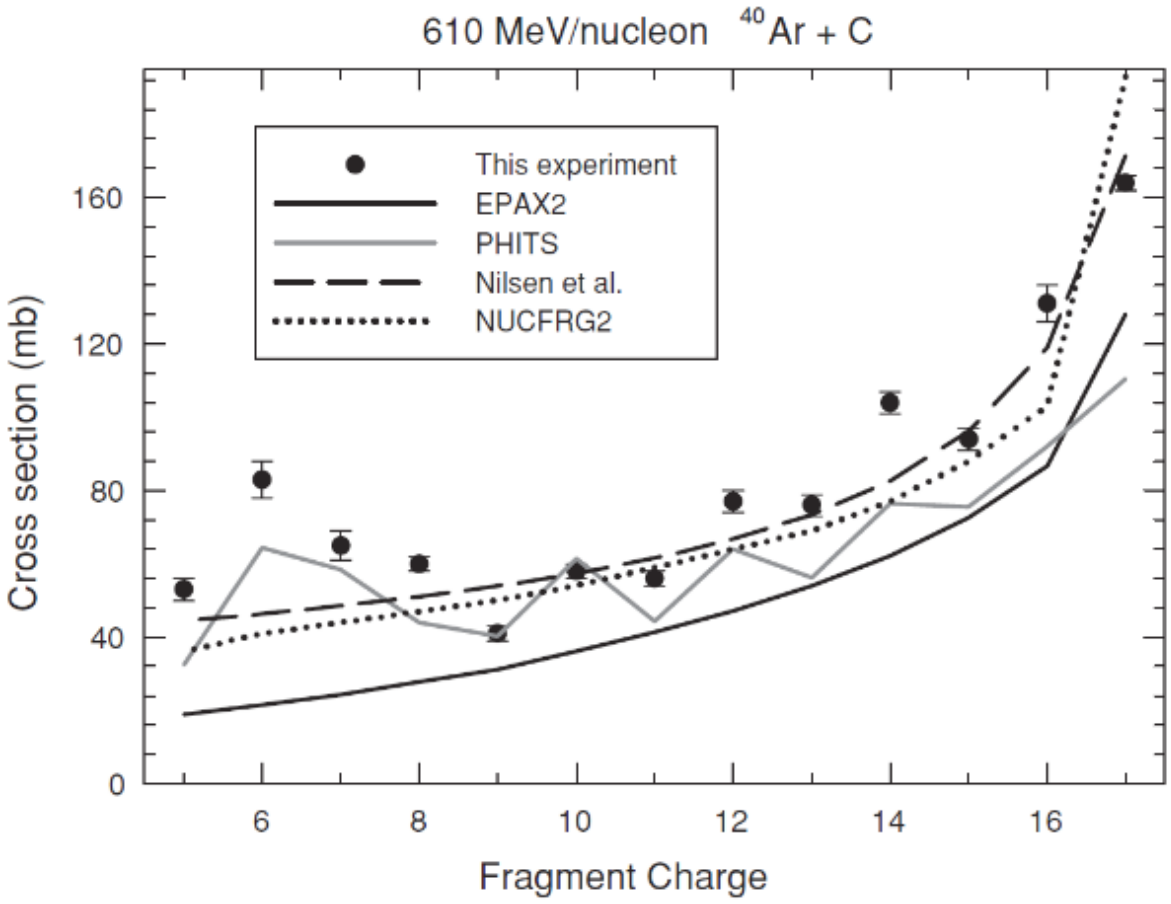

Figure 12: Nuclear fragmentation model cross sections compared to experiment for the 610 MeV/n 40Ar + C reaction. Reprinted from Zeitlin et al. (2008a).

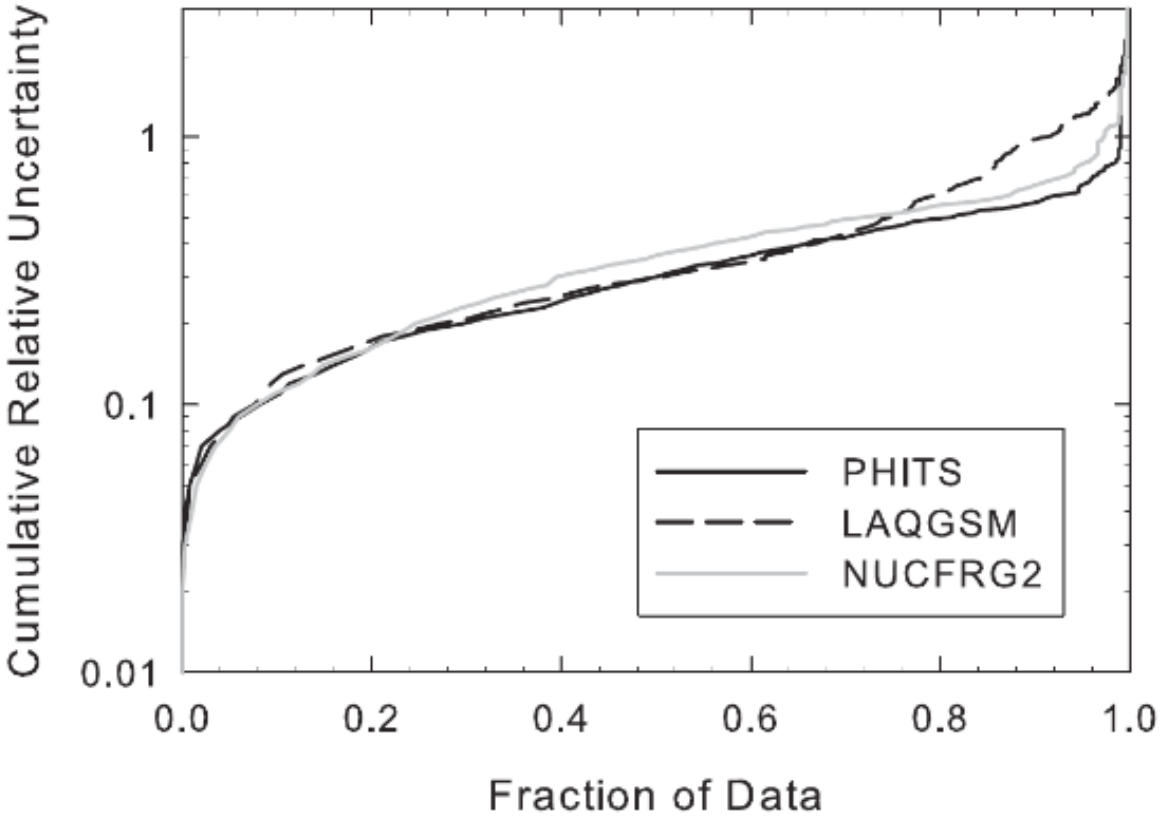

Figure 13: Cumulative relative uncertainty calculated for PHITS, LAQGSM, NUCFRG2 models. Reprinted from Zeitlin et al. (2011).

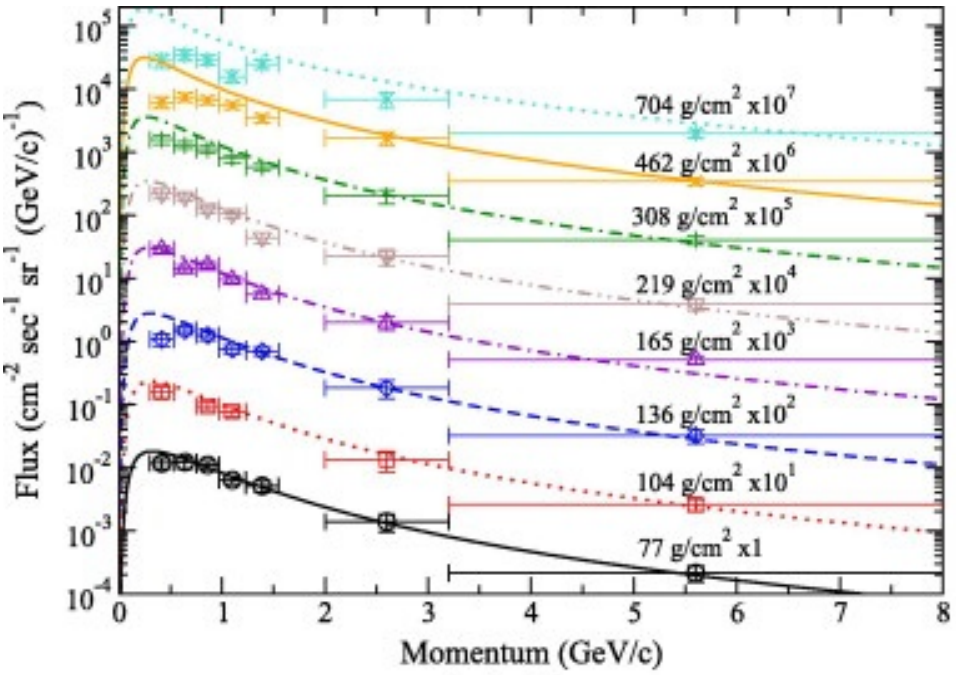

(a)

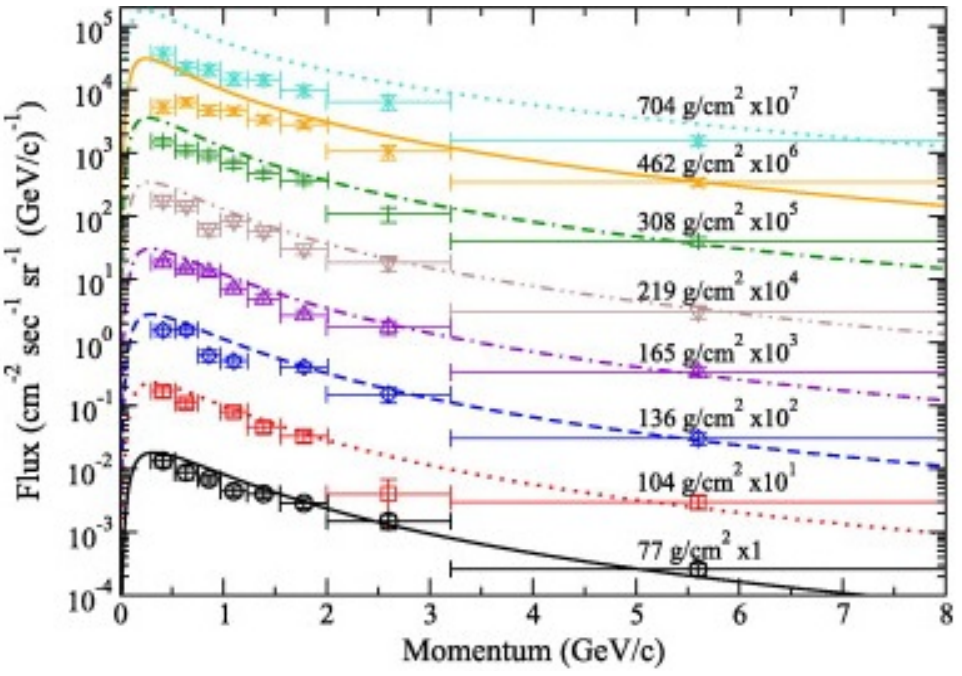

(b)

Figure 14: Comparison of HZETRN results to CAPRICE98 measurements at a range of depths in the atmosphere, for (a) μ^+ and (b) μ^-. Reprinted from Norman et al. (2012).

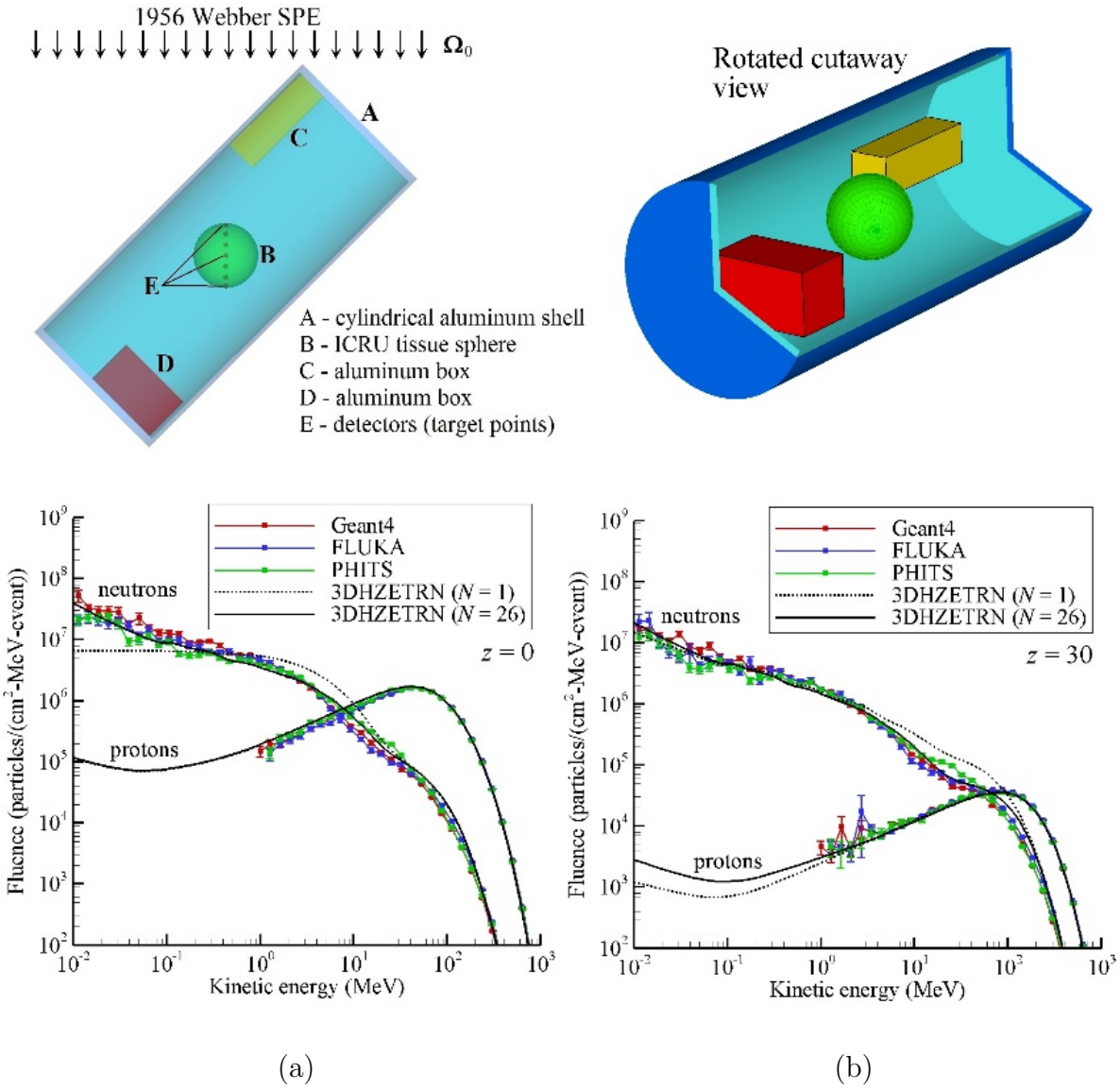

Figure 15: Comparison between 3DHZETRN and Monte Carlo simulation results in combinatorial geometry for the (a) top and (b) bottom of the ICRU tissue sphere. Reprinted from Slaba et al. (2016a).

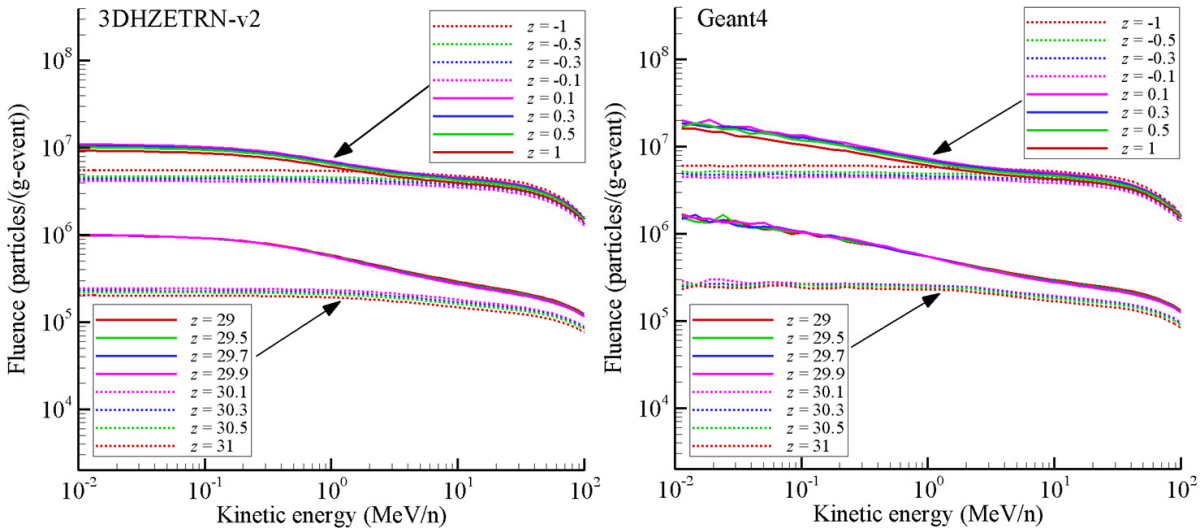

(a) (b)

Figure 16: Scaled proton fluence near the aluminum/water interface in slab geometry with (a) 3DHZETRN and (b) Geant.

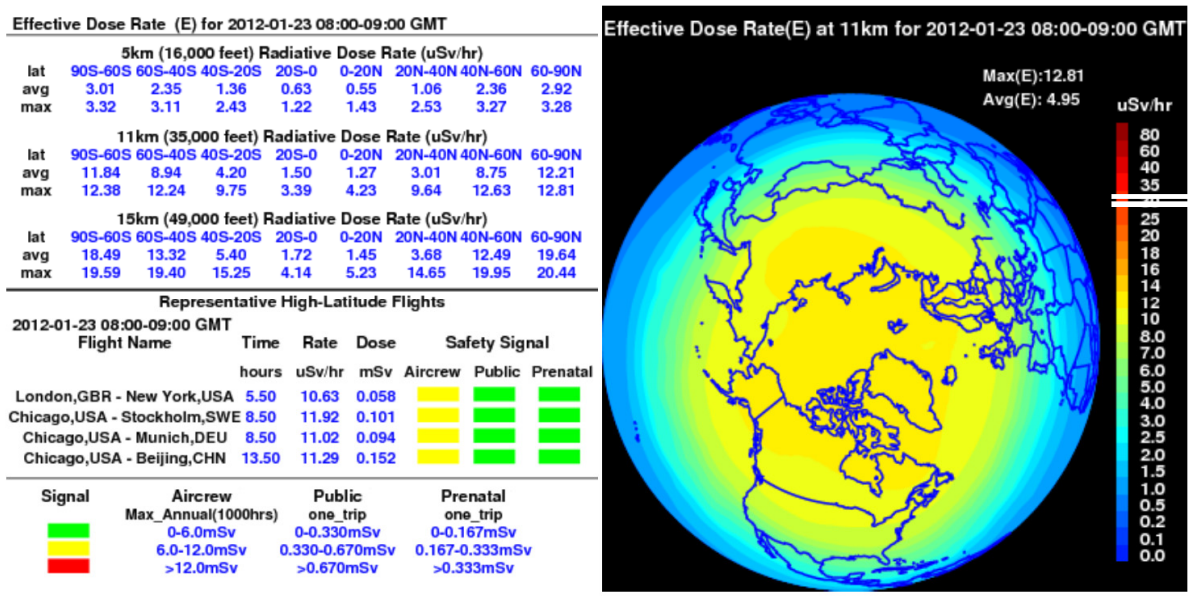

Figure 17: Example tabular/graphical data products from real-time NAIRAS model predictions during the January 2012 SPE events.

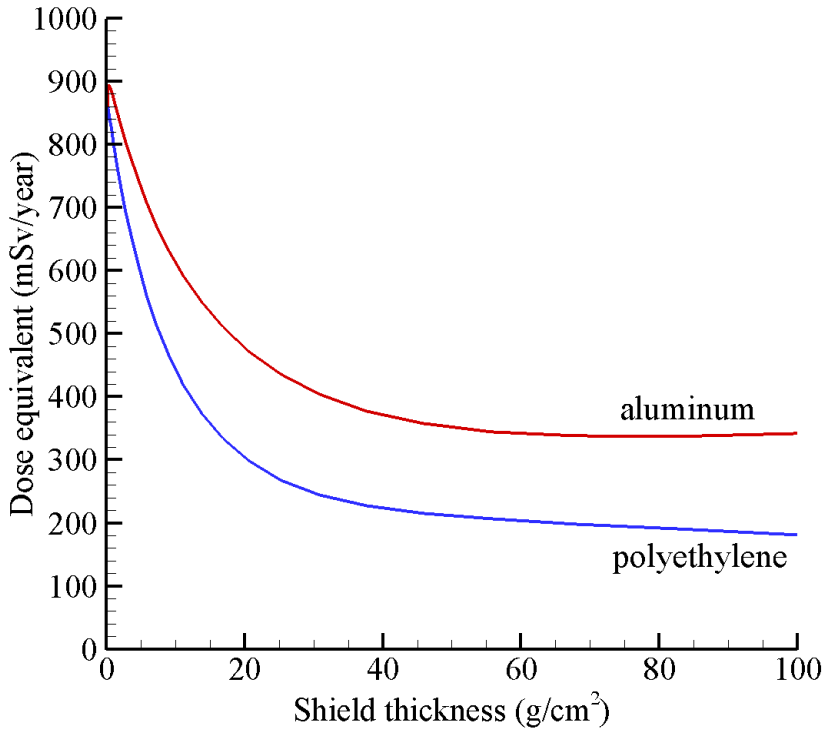

(a)

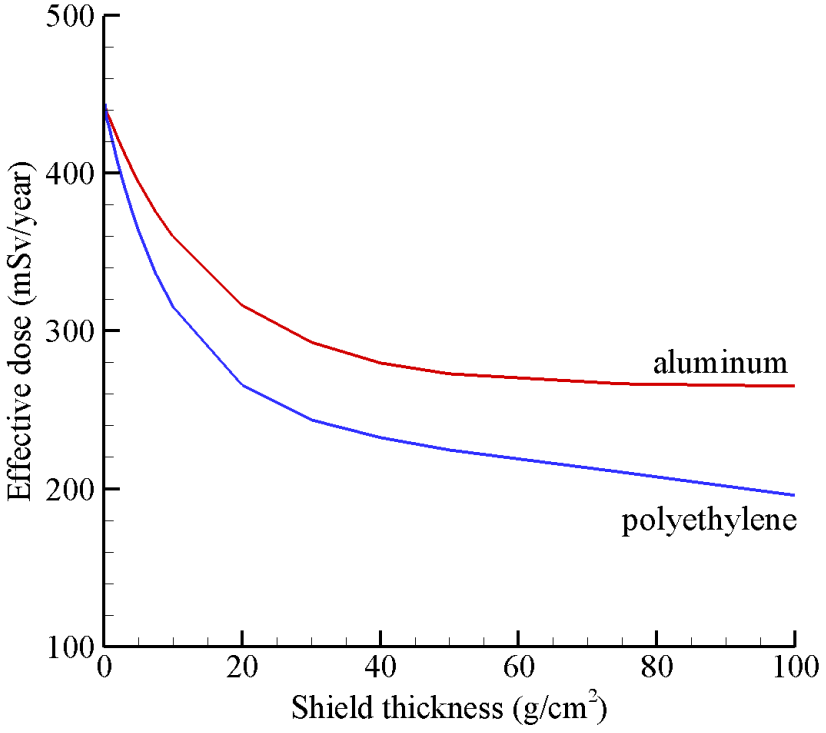

(b)

Figure 18: Annual (a) dose equivalent and (b) effective dose versus shielding thickness for a single planar geometry. The Badhwar-O'Neill 2010 model (O'Neill, 2010) was used to generate the October 1976 GCR environment.

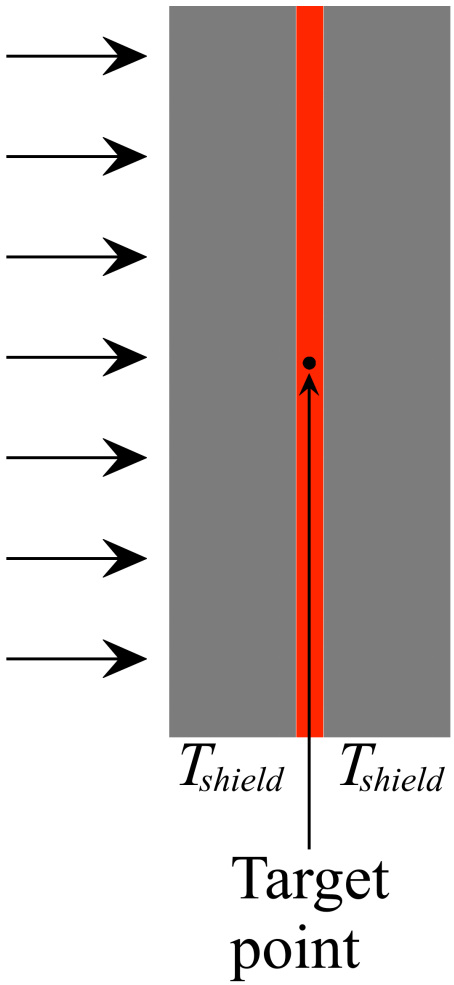

Figure 19: Particles produced in both the front and back shield, and the front and back tissue material contribute to radiation exposure at a target point. The GCR external environment impinges from the left, as shown by the arrows. T_{shield} represents the shield thickness. Reprinted from Slaba et al. (2017).

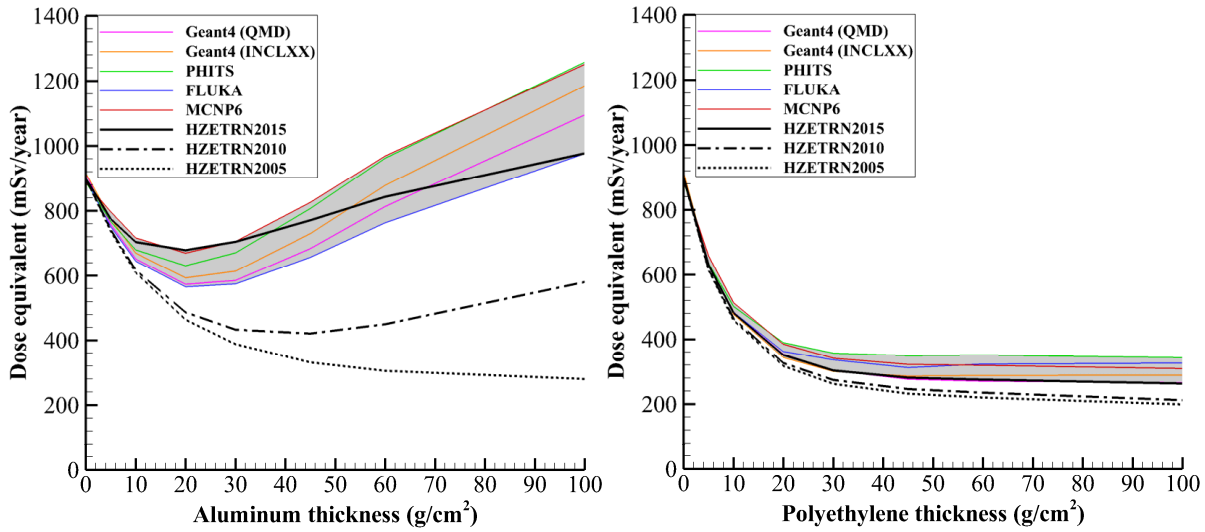

(a) (b)

Figure 20: Annual dose equivalent versus shielding thickness for the front-back shield geometry of Figure 19, with (a) aluminum and (b) polyethylene shielding.

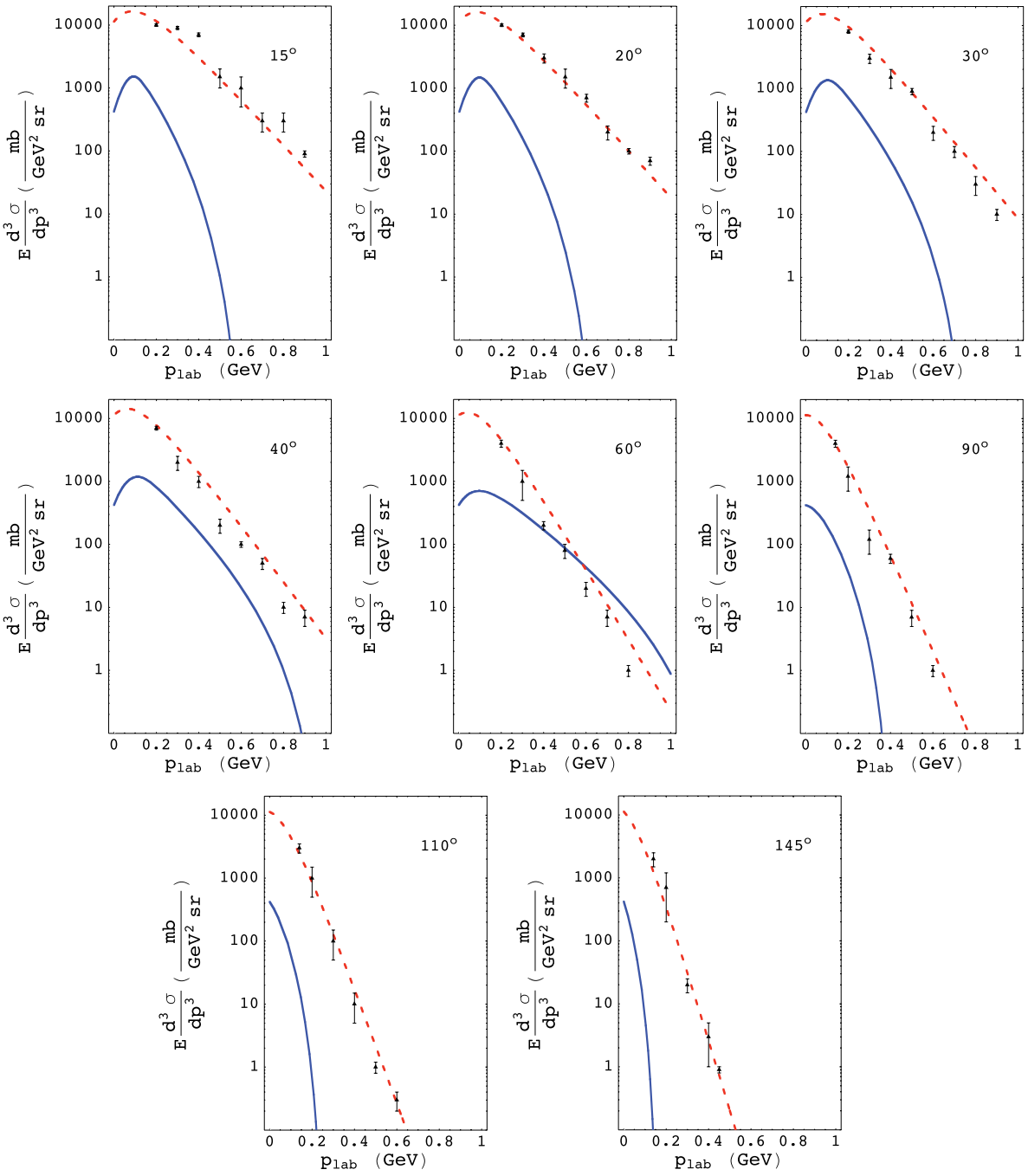

Figure 21: Lorentz-invariant double-differential cross sections for inclusive π^- production in Ar + KCl collisions at 800 MeV/nucleon compared to experimental data (Nagamiya et al., 1981) at a variety of angles. The red dashed lines are the result of a thermal model for π^- production. The blue solid line is the parameterization of Badhwar et al. (1977). Reprinted from Norbury (2011).

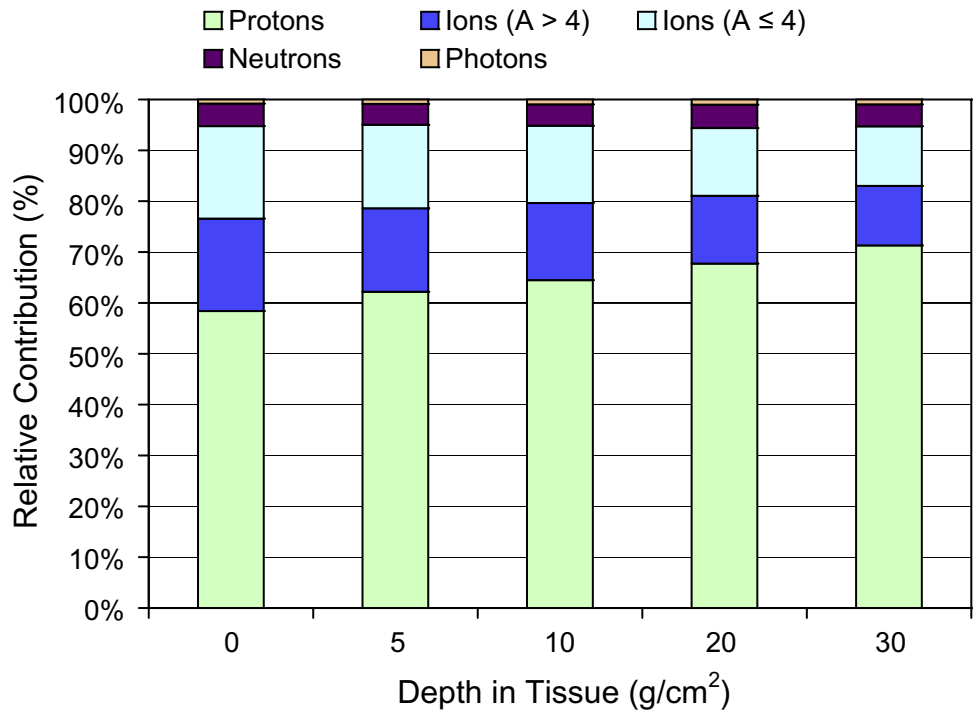

(a)

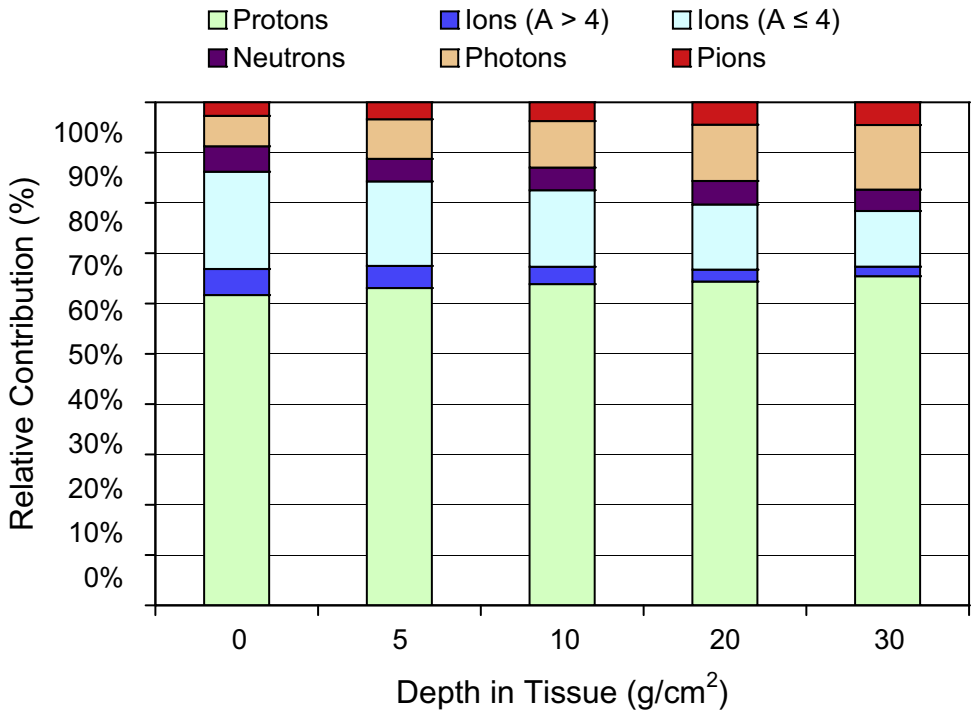

(b)

Figure 22: Relative contribution of various particles to total dose behind 20 g/cm^2 Al shielding plus tissue material. The total pion contribution includes both the pion and photon contributions because the photons result from neutral pion decay. (a) Pion channel turned off, (b) pion channel turned on. Reprinted from Aghara et al. (2009).

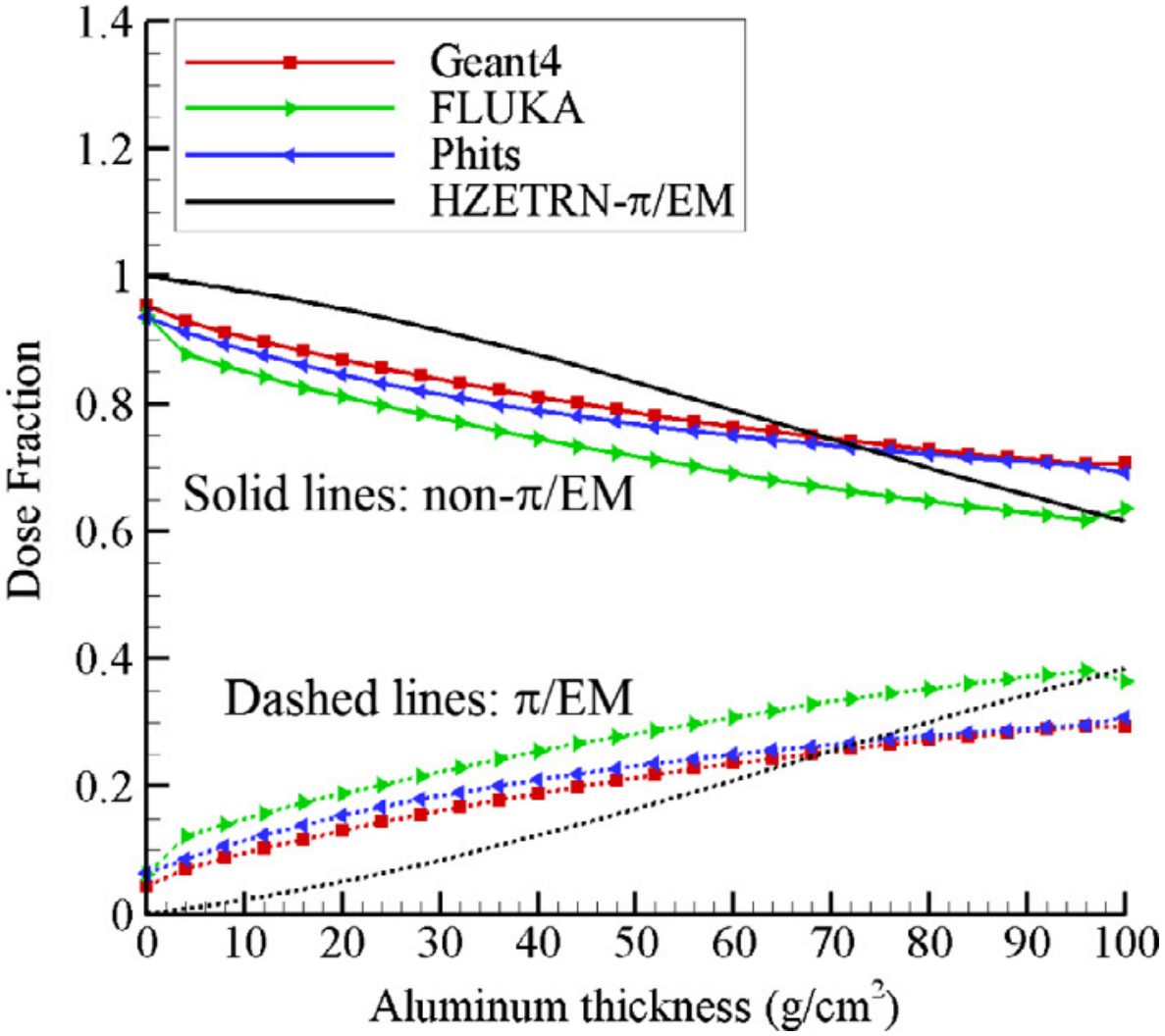

Figure 23: Dose fraction versus depth in 100 g/cm^2 Al slab exposed to a full GCR spectrum, as calculated by various different transport codes. The dashed lines indicate the fraction of dose caused by the pions and subsequent electromagnetic (EM) cascade. The sold lines indicate the fraction of dose by the rest of the particles. Reprinted from Slaba et al. (2013b).

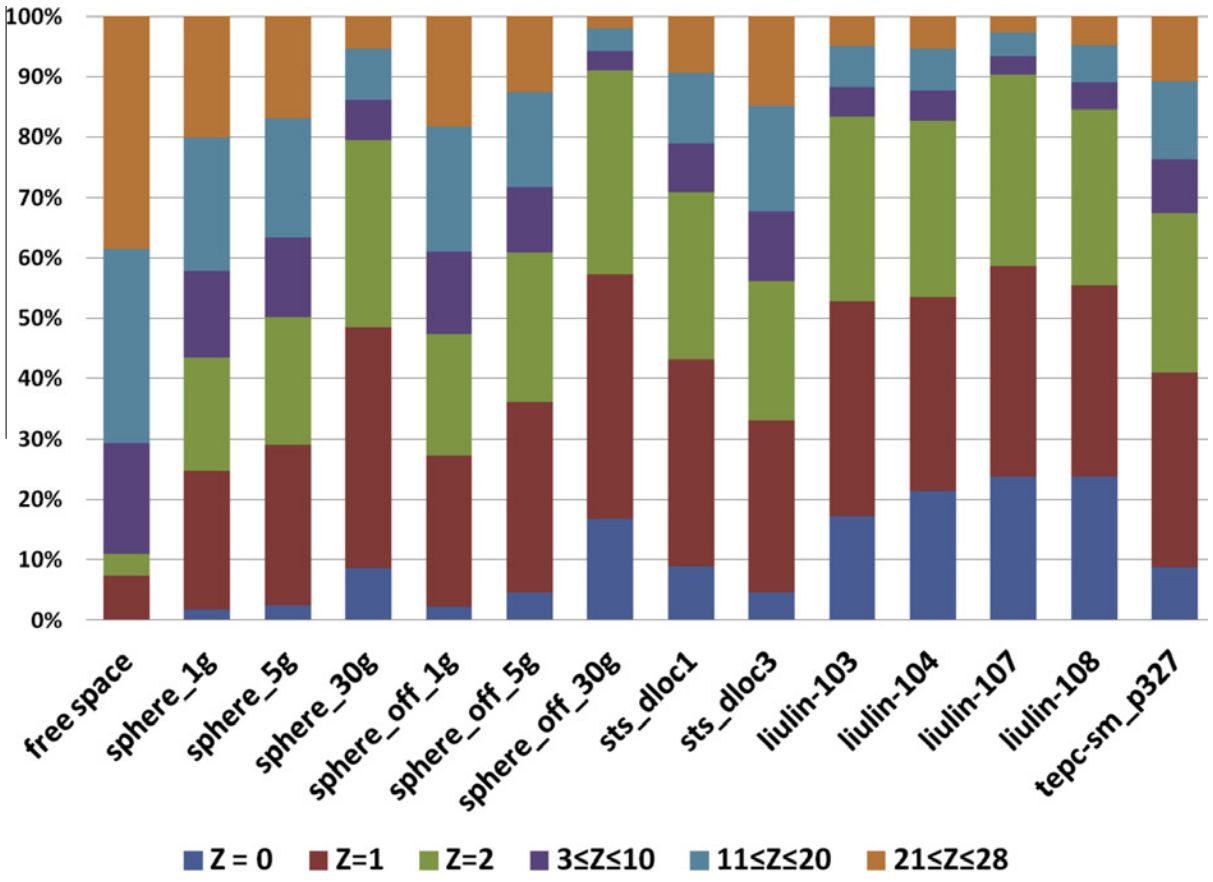

Figure 24: Calculated percent contribution to blood forming organ (BFO) dose equivalent for free space (far left), simple spherical geometries in free space, and detector locations inside the space shuttle (STS) and the International Space Station (ISS) in free space. Reprinted from Walker et al. (2013) and Norbury and Slaba (2014).

References

Adamczyk, A.M., Norbury, J.W., 2011. Electromagnetic dissociation cross sections using Weisskopf-Ewing theory. Nucl. Tech. 175, 216-227.

Adamczyk, A.M., Norman, R.B., Sriprisan, S.I., Townsend, L.W., Norbury, J.W., Blattnig, S.R., Slaba, T.C., 2012. NUCFRG3: Light ion improvements to the nuclear fragmentation model. Nucl. Instr. Meth. Phys. Res. A 678, 21-32.

Adamczyk, A.M., Norbury, J.W., Townsend, L.W., 2013. Weisskopf-Ewing and Hauser-Feshbach calculations of photonuclear cross sections used for electromagnetic dissociation. Rad. Phys. Chem. 90, 21-25.

Adams, J.H., Bhattacharya, M., Lin, Z.W., Pendleton, G., Watts, J.W., 2007. The ionizing radiation environment on the Moon. Adv. Space Res. 40, 338-341.

Aghara, S.K., Blattnig, S.R., Norbury, J.W., Singleterry, R.C., 2009. Monte Carlo analysis of pion contribution to absorbed dose from galactic cosmic rays. Nucl. Instr. Meth. Phys. Res. B 267, 1115-1124.

Aguilar, M., et al., 2015a. Precision measurement of the proton flux in primary cosmic rays from rigidity 1 GV to 1.8 TV with the alpha magnetic spectrometer on the international space station. Phys. Rev. Lett. 114, 171103.

Aguilar, M., et al., 2015b. Precision measurement of the helium flux in primary cosmic rays of rigidities 1.9 GV to 3 TV with the alpha magnetic spectrometer on the international space station. Phys. Rev. Lett. 115, 211101.

Aguilar, M., et al., 2016. Precision measurement of the boron to carbon flux ratio in cosmic rays from 1.9 GV to 2.6 TV with the alpha magnetic spectrometer on the international space station. Phys. Rev. Lett. 117, 231102.

Aguilar et al., 2018. Observation of the fine time structures in the cosmic proton and helium fluxes with the alpha magnetic spectrometer on the international space station. Phys. Rev. Lett 121, 051101.

Ahern, S.C., Norbury, J.W., 2003. A semiclassical electroweak Weiszacker-Williams method. Phys. Rev. D 68, 113001.

Ahern, S.C., Norbury, J.W., 2004. Semiclassical electroweak Weiszacker-Williams method. II. Boson masses and minimum impact parameter. Phys. Rev. D 70, 033008.

American Meteorological Society (AMS), 2007. Integrating space weather observations and forecasts into aviation operations, Washington, DC; 2007.

Badavi, F.F., Nealy, J.E., Wilson, J.W., 2011. The low Earth orbit validation of a dynamic and anisotropic trapped radiation model through ISS measurements. Adv. Space Res. 48, 1441-1458.

Badavi, F.F., 2013. Exposure estimates for repair satellites at geosynchronous orbit, Acta Astro. 83, 18-26.

Badavi, F.F., Walker, S.A., Santos Koos, L.M., 2015. Low Earth orbit assessment of

proton anisotropy using AP8 and AP9 trapped proton models. Life Sci. Space Res. 5, 21-30.

Badhwar, G.D., Stephens, S.A., Golden, R.L., 1977. Analytic representation of the proton-proton and proton-nucleus cross section and its application to the sea level spectrum and charge ratio of muons. Phys. Rev. D 15, 820-831.

Blattnig, S.R., Norbury, J.W., Norman, R.B., Wilson, J.W., Singleterry, R.C., Tripathi, R.K., 2004. MESTRN: A deterministic meson-muon transport code for space radiation. NASA Technical Memorandum 2004-212995.

Bondorf, J.P., Botvina, A., Iljinov, A., Mishustin, I.N., Sneppen, K., 1995. Statistical multifragmentation of nuclei. Phys. Rep. 257, 133-221.

Botvina, A., Chaudhuri, A., Das Gupta, S., Mishustin, I., 2008. Comparison of statistical multifragmentation model simulations with canonical thermodynamic model results: A few representative cases. Phys. Lett. B 668, 414-419.

Cain et al, A proposed model for the international geomagnetic reference Field-1965. 1967. J. Geomag. Geoelec. 19, 335-355.

Clowdsley, M.S., Heinbockel, J.H., Kaneko, H., Wilson, J.W., Singleterry, R.C., Shinn, J.L., 2000. A comparison of the multigroup and collocation methods for solving the low-energy neutron Boltzmann equation. Can. J. Phys. 78, 45-56,

Copeland, K., Sauer, H.H. Duke, F.E. Friedberg, W., 2008. Cosmic radiation exposure on aircraft occupants on simulated high-latitude flights during solar proton events from 1 January 1986 through 1 January 2008. Adv. Space Res. 42, 1008-1029.

Cucinotta, F.A., Kim, M.Y., Schneider, S.I., Hassler, D.M., 2007. Description of light ion production cross sections and fluxes on the Mars surface using QMSFRG model. Rad. Environ. Biophys. 46, 101-106.

Cucinotta, F.A., Kim, M.Y., Chappell, L.J., 2013. Space radiation cancer risk projections and uncertainties - 2012. NASA Technical Paper 2013-217375.

David, J.C., 2015. Spallation reactions: A successful interplay between modeling and applications. Eur. Phys. J. A 51, 68-125.

Das, C.B., Das Gupta, S., Lynch, W.G., Mekjian, A.Z., Tsang, M.B., 2005. The thermodynamic model for nuclear fragmentation. Phys. Rep. 406, 1-47.

Dyer, C., Hands, A., Lei, F., Truscott, P., Ryden, K.A., Morris, P., Getley, I., Bennett, L., Bennett, B., Lewis, B., 2009. Advances in measuring and modeling the atmospheric radiation environment. IEEE Trans. Nucl. Sci. 56, 3415-3422.

Feynman, J., Ruzmaikin, A., Berdichevsky, V., 2002. The JPL proton fluence model: An update. J. Atmos. Solar Terrestrial Phys. 64, 1679-1686.

Fisher, G., 2009. Lessons from aviation: Linking space weather science to decision making. Space Weather 7, S03005.

Ginet G.P., O'Brien, T.P., Huston, S.L., Johnston, W.R., Guild, T.B., Friedel, R., Lindstrom, C.D., Roth, C.J., Whelan, P., Quinn, R.A., Madden, D., Morley, S., Yi-Jiun, S., 2013. AE9, AP9 and SPM: New models for specifying the trapped energetic particle and space plasma environment. Space Sci. Rev. 179, 579-615.

Guo, J., Slaba, T.C., Zeitlin, C., Wimmer-Schweingruber, R.F., Bohm, E., Bottcher, S., Brinza, D.E, Ehresmann, B., Hassler, D.M., Matthia, D., Rafkin, S., 2017.

Dependence of the Martian radiation environment on atmospheric depth: Modeling and measurement. J. Geophys. Res. - Planets 122, 329-341.

Gronoff, G., Norman, R.B., Mertens, C.J., 2015. Computation of cosmic ray ionization and dose at Mars I: A comparison of HZETRN and Planetocosmics for protons and alpha particles. Adv. Space Res. 55, 1799-1805.

Hassler, D.M., Norbury, J.W., Reitz, G., 2017. Mars science laboratory radiation assessment detector (MSL/RAD) modeling workshop proceedings. Life Sci. Space Res. 14, 1-2.

Hayatsu, K., Hareyama, M., Kobayashi, S., Yamashita, N., Miyajima, M., Sakurai, K., Hasebe, N., 2008. Radiation doses for humans exposed to galactic cosmic rays and their secondary products on the lunar surface. Bio. Sci. Space 22, 59-66.

Heilbronn, L.H., Borak, T.B., Townsend, L.W., Tsai, P., Burnham, C.A., McBeth, R.A., 2015. Neutron yields and effective doses produced by galactic cosmic ray interactions in shielded environments in space. Life Sci. Space Res. 7, 90-99.

Heinbockel, J.H., Slaba, T.C., Blattnig, S.R., Tripathi, R.K., Townsend, L.W., Handler, T., Gabriel, T.A., Pinsky, L.S., Reddell, B., Clowdsley, M.S., Singleterry, R.C., Norbury, J.W., Badavi, F.F., Aghara, S.K., 2011a. Comparison of the transport codes HZETRN, HETC and FLUKA for a solar particle event. Adv. Space Res. 47, 1079-1088.

Heinbockel, J.H., Slaba, T.C., Tripathi, R.K., Blattnig, S.R., Norbury, J.W., Badavi, F.F., Townsend, L.W., Handler, T., Gabriel, T.A., Pinsky, L.S., Reddell, B., Aumann, A.R., 2011b. Comparison of the transport codes HZETRN, HETC and FLUKA for galactic cosmic rays. Adv. Space Res. 47, 1089-1105.

ICRP, 1991. ICRP Publication 60: 1990 Recommendations of the International Commission on Radiological Protection. Pergamon Press, Oxford, U.K. 1991.

ICRP, 2007. ICRP Publication 103: 2007 Recommendations of the International Commission on Radiological Protection. New York, NY; 2007.

ICRP, 2013. International Commission on Radiological Protection: ICRP Publication 123: Assessment of radiation exposure of astronauts in space. Plestar Wheatons Ltd., Exeter, U.K. 2013.

ICRU, 2010. International Commission on Radiation Units and Measurements: ICRU Report 84, Reference data for the validation of doses from cosmic-radiation exposure of aircraft crew. J. ICRU, 10, Oxford University Press, Oxford, U.K. 2010.

ISO, 2004. International Standardization Organization: Space environment (natural and artificial) - galactic cosmic ray model. ISO 15390.

Jensen, D.C., Cain, J.C., 1962. An interim geomagnetic field. J. Geophys. Res. 67, 3568-3569.

Kim, M.Y., Hayat, M.J., Feiveson, A.H., Cucinotta, F.A., 2009. Prediction of frequency and exposure level of solar particle events. Health Phys. 97, 68-81.

Kim, M.Y., Rusek, A., Cucinotta, F.A., 2015. Issues for simulation of galactic cosmic ray exposures for radiobiological research at ground based accelerators. Front. Oncol. 5, 122.

Kim, M.Y., Blattnig, S.R., Clowdsley, M.S., Norman, R.B., 2017. Using spectral

shape and predictor fluence to evaluate temporal dependence of exposures from solar particle events. Space Weather 15, 374-391.

King, J.H., 1974. Solar proton fluences for 1977-1983 space missions. J. Spacecraft Rockets 11(6), 401-408.

Kress, B.T., Mertens, C.J., Wiltberger, M., 2010. Solar energetic particle cutoff variations during the 29-31 October 2003 geomagnetic storm. Space Weather 8, S05001.

Kuznetsov, N.V., Popova, H., Panasyuk, M.I., 2017. Empirical model of long-time variations of galactic cosmic ray particle fluxes. J. Geophys. Res. Space Phys. 115, 1463-1475.

Lindborg, L., Bartlett, D.T., Beck, P., McAulay, I., Schnuer, K., Straube, H., Spurney, F. (editors), 2004. Cosmic radiation exposure of aircraft crew. Compilation of measured and calculated data. Final report of the EURADOS WG 5 to the group of experts established under article 31 of the European commission, Directorate general for energy and transportation. Radiation Protection Issue No. 140, Luxembourg; 2004.

Lovelace, A.M., Rashid, A.M., de Wet, W.C., Townsend L.W., Hines, J.W., Moussa, H., 2018. Solar particle event dose forecasting using regression techniques. Space Weather 16, 1073-1085.

Martucci et al., 2018. Proton fluxes measured by the PAMELA experiment from the minimum to the maximum solar activity for solar cycle 24. Astrophys. J. Lett. 854, L2.

Matthia, D., Berger, D., Mrigakshi, A.I., Reitz, G., 2013. A Ready-to-use galactic cosmic ray model. Adv. Space Res. 51, 329-338.

Matthia, D., Ehresmann, B., Lohf, H., Kohler, J., Zeitlin, C., Appel, J., Sato, T., Slaba, T.C., Martin, C., Berger, T., Boehm, E., Boettcher, S., Brinza, D.E., Burmeister, S., Guo, J., Hassler, D.M., Posner, A., Rafkin, S.C.R., Reitz, G., Wilson, J.W., Wimmer-Schweingruber, R.F., 2016. The Martian surface radiation environment - a comparison of models and MSL/RAD measurements. J. Space Weather Space Clim. 6, A13.

Matthia, D., Hassler, D.M., de Wet, W., Ehresmann, B., Firan, A., Flores-McLaughlin, J., Guo, J., Heilbronn, L.H., Lee, K., Ratliff, H., Rios, R.R., Slaba, T.C., Smith, M., Stoffle, N.N., Townsend, L.W., Berger, T., Reitz, G., Wimmer-Schweingruber, R.F., Zeitlin, C., 2017. The radiation environment on the surface of Mars - summary of model calculations and comparison to RAD data. Life Sci. Space Res. 14, 18-28.

McCormack, P.D., 1988. Radiation dose and shielding for the space station. Acta Astro. 17, 231-241.

McKinney, G.W., Lawrence, D.J., Prettyman, T.H., Elphic, R.C., Feldman, W.C., Hagerty, J.J., 2006. MCNPX benchmark for cosmic ray interactions with the Moon. J. Geophys. Res. 111, E06004.

Mertens, C.J., Kress, B.T., Wiltberger, M., Blattnig, S.R., Slaba, T.C., Solomon, S.C., Engel, M., 2010. Geomagnetic influence on aircraft radiation exposure during a solar energetic particle event in October 2003. Space Weather 8, S03006..

Mertens, C.J., Kress, B.T., Wiltberger, M., Tobiska, W.K., Grajewski, B., Xu, X.,

2012. Atmospheric ionizing radiation from galactic and solar cosmic rays. Current Topics in Ionizing Radiation Research, edited by Mitsuru Nenoi, InTech Publisher Rijeka, Croatia.

Mertens, C.J., Meier, M.M., Brown, S., Norman, R.B., Xu, X., 2013. NAIRAS aircraft radiation model development, dose climatology, and initial validation. Space Weather 11, 1-33.

Mertens. C.J., 2016. Overview of the radiation dosimetry experiment (RaD-X) flight campaign. Space Weather 14, 874-898.

Mertens, C.J., 2016a. Overview of the radiation dosimetry experiment (RaD-X) flight mission. Space Weather 14, 921-934.

Mertens, C.J., Grono, G.P., Norman, R.B., Hayes, B.M., Lusby, T.C., Straume, T., Tobiska, W.K., Hands, A., Ryden, K., Benton, E., Wiley, S., Gersey, B., Wilkins, R., Xu, X., 2016b. Cosmic radiation dose measurements from the RaD-X flight campaign. Space Weather 14, 874-898.

Mertens, C.J., Slaba, T.C., Hu, S., 2018. Active dosimeter-based estimate of astronaut acute radiation risk for real-time solar energetic particle events. Space Weather 16, 1291-1316.

Mrigakshi, A.I., Matthia, D., Berger, T., Reitz, G., Wimmer-Schweingruber, R.W., 2012. Assessment of galactic cosmic ray models. J. Geophys. Res. Space Phys. 117, A08109.

Nagamiya, S. Lemaire, M.C. Moeller, E. Schnetzer, S. Shapiro, G. Steiner, H. Tanihata, I., 1981. Production of pions and light fragments at large angles in high energy nuclear collisions. Phys. Rev. C 24, 971-1009.

NASA, 2006. National Aeronautics and Space Administration: NASA standard for models and simulations. NASA-STD-7009, Washington D.C.,

NASA, 2007. National Aeronautics and Space Administration: NASA Space Flight Human System Standard. Crew Health, vol. 1. NASA-STD-3001, Washington D.C.

NASA, 2015. Cross-program design specification for natural environments (DSNE). SLS-SPEC-159, Revision C.

NCRP, 2002. National Council on Radiation Protection and Measurements: Operational radiation safety program for astronauts in low-Earth orbit: A basic framework. NCRP Report No. 142, Bethesda, Maryland.

NCRP, 2009. National Council on Radiation Protection and Measurements: Ionizing radiation exposure of the population of the United States. NCRP Report No. 160, Bethesda, Maryland.

NCRP, 2014. National Council on Radiation Protection and Measurements: Radiation protection for space activities: supplement to previous recommendations. NCRP Commentary No. 23. Bethesda, Maryland.

Nealy, J.E., Chang, C.K., Norman, R.B., Blattnig, S.R., Badavi, F.F., Adamczyk, A.M., 2010. A deterministic computational procedure for space environment electron transport. Nucl. Instr. Meth. Phys. Res. B 268, 2415-2425.

Norbury, J.W., 2006. Pair production from nuclear collisions and cosmic ray transport.

J. Phys. G 32, B31-35.
Norbury, J.W., Maung K.M., 2007. Electromagnetic dissociation and space radiation. Acta Astro. 60, 770-774.
Norbury, J.W., 2009a. Parameterizations of inclusive cross sections for kaon, proton and antiproton production in proton - proton collisions. Astrophys. J. Suppl. 182, 120-126.
Norbury, J.W., 2009b. Total cross section parameterizations for pion production in nucleon - nucleon collisions. Nucl. Inst. Meth. Phys. Res. B 267, 1209-1212.
Norbury, J.W., 2009c. Pion cross section parameterizations for intermediate energy nucleus - nucleus collisions. Phys. Rev. C 79, 037901.
Norbury, J.W., 2011. Erratum: Pion cross section parameterizations for intermediate energy nucleus - nucleus collisions. Phys. Rev. C 83, 059903.
Norbury, J.W., Miller, J., 2012. Review of nuclear physics experimental data for space radiation. Health Phys. 103, 640-642.
Norbury, J.W., Miller, J. Adamczyk, A.M., Heilbronn, L.H., Townsend, L.W., Blattnig, S.R., Norman, R.B., Guetersloh, S.B., Zeitlin, C.J., 2012. Nuclear data for space radiation. Rad. Meas. 47, 315-363.
Norbury, J.W., 2013. Light ion and multiple nucleon removal due to electromagnetic dissociation. Nucl. Instr. Meth. Phys. Res. A 703, 220-243.
Norbury, J.W., Slaba T.C., 2014. Space radiation accelerator experiments - The role of neutrons and light ions. Life Sci. Space Res. 3, 90-94.
Norbury, J.W., et al., 2016. Galactic cosmic ray simulation at the NASA space radiation laboratory. Life Sci. Space Res. 8, 38-51.
Norbury, J.W., Slaba, T.C., Sobolevsky, N., Reddell, B.D., 2017. Comparing HZETRN, SHIELD, FLUKA, and GEANT Transport Codes. Life Sci. Space Res. 14, 64-73.
Norbury, J.W., Whitman, K., Lee, K., Slaba, T.C., Badavi, F.F., 2018a. Comparison of space radiation GCR models to recent AMS data. Life Sci. Space Res. 18, 64-71.
Norbury, J.W., Slaba, T.C., Sobolevsky, N., Werneth, C.M., 2018b. SHIELD and HZETRN comparisons of pion production cross sections Nucl. Instr. Meth. Phys. Res. B 418, 13-17.
Norman, R.B., Blattnig, S.R., De Angelis, G., Badavi, F.F., Norbury, J.W., 2012. Deterministic pion and muon transport in Earth's atmosphere. Adv. Space Res. 50, 146-155.
Norman, R.B., Blattnig, S.R., 2013. Validation of nuclear models used in space radiation shielding applications. J. Comp. Phys. 233, 464-479.
Norman, R.B., Slaba, T.C., Blattnig, S.R., 2013. An extension of HZETRN for cosmic ray initiated electromagnetic cascades. Adv. Space Res. 51, 2251-2260.
Norman, R.B, Gronoff, G., Mertens, C.M., 2014. Influence of dust loading on atmospheric Ionizing radiation on Mars. J. Geophys. Res. Space Physics 119, 452-461.
Norman, R.B., Mertens, C.J., Slaba, T.C., 2016. Evaluating galactic cosmic ray environment models using RaD-X flight data. Space Weather 14, 764-775.
NRC, 2008. National Research Council: Managing space radiation risk in the new era of space exploration. National Academy of Sciences Press, Washington D.C.

NRC, 2012. National Research Council: Committee for evaluation of space radiation cancer risk model: Technical evaluation of the NASA model for cancer risk to astronauts due to space radiation. National Academy of Sciences Press, Washington D.C.

Nymmik, R.A., Panasyuk, M.I., Pervaya, T.I., Suslov, A.A., 1992. A model of galactic cosmic ray fluxes. Nucl. Tracks Rad. Meas. 20, 427-429.

Nymmik, R.A., Panasyuk, M.I., Pervaya, T.I., Suslov, A.A., 1994. An analytical model describing dynamics of galactic cosmic ray heavy particles. Adv. Space Res. 14, 759-763.

Nymmik, R.A., Panasyuk, M.I., Suslov, A.A., 1996. Galactic cosmic ray flux simulation and prediction. Adv. Space Res. 17, 219-230.

O'Neill, P.M., 2006. Badhwar-O'Neill galactic cosmic ray model updated based on Advanced Composition Explorer (ACE) energy spectra from 1997 to present. Adv. Space Res. 37, 1727-1733.

O'Neill, P.M., 2010. Badhwar-O'Neill galactic cosmic ray flux model - revised. IEEE Trans. Nucl. Sci. 57, 3148-3153.

O'Neill, P.M., Golge, S., Slaba, T.C., 2015. Badhwar-ONeill 2014 galactic cosmic ray flux model description. NASA Technical Paper 2015-218569.

Pesnell, W.D., 2012. Solar cycle predictions. Solar Physics 281, 507-532.

Petti, P.L., Lennox, A.J., 1994. Hadronic radiotherapy. Ann. Rev. Nucl. Part. Sci. 44, 155-197.

Pshenichonov, I., Botvina, A., Mishustin, I., Greiner, W., 2010. Nuclear fragmentation reactions in extended media studied with Geant4 toolkit. Nucl. Instr. Meth. Phys. Res. B 268, 604-615.

PourArsalan, M., Townsend, L.W., 2013. Emitted high energy light particle data base development using a thermodynamic coalescence model. J. Phys. G. Conf. Ser. 420, 012063.

Sawyer, D.M., Vette, J.I., 1976. AP8 trapped proton environments for solar maximum and solar minimum. National Space Science Data Center, World Data Center A for Rockets and Satellites, NSSDC/WDC-A-R&S 76-06.

Shavers, M.R., Frankel, K., Miller, J., Schimmerling, W., Townsend, L.W., Wilson, J.W., 1993. The fragmentation of 670 A MeV Neon-20 as a function of depth in water. III. Analytic multigeneration transport theory. Rad. Res. 134, 1-14.

Simpson, J.A., 1983. Elemental and isotopic composition of the galactic cosmic rays. Ann. Rev. Nucl. Part. Sci. 33, 323-381.

Singleterry, R.C., Wilson, J.W., Shinn, J.L., Tripathi, R.K., Thibeault, S.A., Noor, A.K., Cucinotta, F.A., Badavi, F.F., Chang, C.K., Qualls, G.D., Clowdsley, M.S., Kim, M.H., Heinbockel, J.H., Norbury, J., Blattnig, S.R., Miller, J., Zeitlin, C., Heilbronn, L.H., 2001. Creation and utilization of a world wide web based space radiation effects code: SIREST. Phys. Med. 17, 90-93.

Singleterry, R.C., Blattnig, S.R., Clowdsley, M.S., Qualls, G.D., Sandridge, C.A., Simonsen, L.C., Slaba, T.C., Walker, S.A., Badavi, F.F., Spangler, J.L., Aumann, A.R., Zapp, E.N., Rutledge, R.D., Lee, K.T., Norman, R.B., Norbury, J.W., 2011.

OLTARIS: On-line tool for the assessment of radiation in space. Acta Astro. 68, 1086-1097.

Slaba, T.C., Blattnig, S.R., Badavi, F.F., 2010a. Faster and more accurate transport procedures for HZETRN. J. Comp. Phys. 229, 9397-9417.

Slaba, T.C., Blattnig, S.R., Aghara, S.K., Townsend, L.W., Handler, T., Gabriel, T.A., Pinsky, L.S., Reddell, B., 2010b. Coupled neutron transport for HZETRN. Rad. Meas. 45, 173-182.

Slaba, T.C., Blattnig, S.R., Clowdsley, M.S., Walker, S.A., Badavi, F.F., 2010c. An improved neutron transport algorithm for HZETRN. Adv. Space Res. 46, 800-810.

Slaba, T.C., Qualls, G.D., Clowdsley, M.S., Blattnig, S.R., Walker, S.A., Simonsen, L.C., 2010d. Utilization of CAM, CAF, MAX, and FAX for space radiation analyses using HZETRN. Adv. Space Res. 45, 866-883.

Slaba, T.C., Blattnig, S.R., Badavi, F.F., Stoffle, N.N., Rutledge, R.D., Lee, K.T., Zapp, E.N., Dachev, Ts. P., Tomov, B.T., 2011a. Statistical validation of HZETRN as a function of vertical cutoff rigidity using ISS measurements. Adv. Space Res. 47, 600-610.

Slaba, T.C., Blattnig, S.R., Clowdsley, M.S., 2011b. Variations in lunar neutron dose estimates. Rad. Res. 176, 837-841.

Slaba, T.C., Blattnig, S.R., Reddell, B., Bahadori, A., Norman, R.B., Badavi, F.F., 2013a. Pion and electromagnetic contribution to dose: Comparisons of HZETRN to Monte Carlo results and ISS data. Adv. Space Res. 52, 62-78.

Slaba, T.C., Mertens, C.J., Blattnig, S.R., 2013b. Radiation shielding optimization on Mars. NASA Technical Paper 2013-217983.

Slaba, T.C., Blattnig, S.R., Tweed, J., 2013c. Reduced discretization error in HZETRN. J. Comp. Phys. 234, 217-229.

Slaba, T.C., 2013d. Faster heavy ion transport for HZETRN. NASA Technical Paper 2013-217803.

Slaba, T.C., Blattnig, S.R., 2014a. GCR environmental models I: Sensitivity analysis for GCR environments. Space Weather 12, 217-224.

Slaba, T.C., Blattnig, S.R., 2014b. GCR environmental models II: Uncertainty propagation methods for GCR environments. Space Weather 12, 225-232.

Slaba, T.C., Xu, X., Blattnig, S.R., Norman, R.B., 2014c. GCR environmental models III: GCR model validation and propagated uncertainties in effective dose. Space Weather 12, 233-245.

Slaba, T.C., Wilson, J.W., Badavi, F.F., Reddell, B.D., Bahadori, A.A., 2016a. Solar proton exposure of an ICRU sphere within a complex structure: Ray-trace geometry. Life Sci. Space Res. 9, 77-83.

Slaba, T.C., Blattnig, S.R., Norbury, J.W., Rusek, A., La Tessa, C., 2016b. Reference field specification and preliminary beam selection strategy for accelerator-based GCR simulation. Life Sci. Space Res. 8, 52-67.

Slaba, T.C., Stoffle, N.N., 2017. Evaluation of HZETRN on the Martian surface: Sensitivity tests and model results. Life Sci. Space Res. 14, 29-35.

Slaba, T.C., Bahadori, A.A., Reddell, B.D., Singleterry, R.C., Clowdsley, M.S., Blat-

tnig, S.R., 2017. Optimal shielding thickness for galactic cosmic ray environments. Life Sci. Space Res. 12, 1-15.

Smart, D.F., Shea, M.A., 1983. Geomagnetic Transmission Functions for 400 km Altitude Satellite: In 18th International Cosmic Ray Conference-Conference Papers MG Sessions, vol. 3. Tata Institute of Fundamental Research, Colaba, Bombay, 419-422.

Smart, D.F., Shea, M.A., 2009. Fifty years of progress in geomagnetic cutoff rigidity determinations. Adv. Space Res. 44, 1107-1123.

Stormer, C. 1937. On the trajectories of electric particles in the field of a magnetic dipole with applications to the theory of cosmic radiation. Astrophys. Norvegica II 4, 193-248.

Straume, T., Mertens, C.J., Lusby, T.C., Gersey, B., Tobiska, W.K., Norman, R.B., Gronoff, G.P., Hands, A., 2016. Ground-based evaluation of dosimeters for NASA high-altitude balloon flight. Space Weather 14, 1011-1025.

Tobiska, W. K., Atwell, W., Beck, P., Benton, E., Copeland, K., Dyer, C., Gersey, B., Getley, I., Hands, A., Holland, M., Hong, S., Hwang, J., Jones, B., Malone, K., Meier, M.M., Mertens, C.J., Phillips, T., Ryden, K., Schwadron, N., Wender, S.A., Wilkins, R., Xapsos, M.A., 2015. Advances in atmospheric radiation measurements and modeling needed to improve air safety, Space Weather 13, 202-210.

Townsend, L.W., Adams, J.H., Blattnig, S.R., Clowdsley, M.S., Fry, D.J., Jun, I., McLeod, C.D., Minow, J.I., Moore, D.F., Norbury, J.W., Norman, R.B., Reames, D.V., Schwadron, N.A., Semones, E.J., Singleterry, R.C., Slaba, T.C., Werneth, C.M., Xapsos, M.A., 2018. Solar particle event storm shelter requirements for missions beyond low Earth orbit. Life Sci. Space Res. 17, 32-39.

Tripathi, R.K., Cucinotta, F.A., Wilson, J.W., 1999. Universal parameterization of absorption cross sections. NASA Technical Paper 209726.

Tylka, A.J., Adams, J.H., Boberg, P.R., Brownstein, B., Dietrich, W.F., Flueckiger, E.O., Peterson, E.L., Shea, M.A., Smart, D.F., Smith, E.C., 1997. CREME96: A revision of the cosmic ray effects on micro-electronics code. IEEE Trans. Nucl. Sci. 44, 2150-2160.

Tylka, A.J., Dietrich, W.F., Atwell, W.A., 2010. Band function representation of solar proton spectra in ground-level events. In: 38th Scientific Assembly of the Committee on Space Research (COSPAR), Bremen, Germany, July 18-25.

Walker, S.A., Townsend, L.W., Norbury, J.W., 2013. Heavy ion contributions to organ dose equivalent for the 1977 galactic cosmic ray spectrum. Adv. Space Res. 51, 1792-1799.

Werneth, C.M., Maung, K.M., 2013. Nucleus-nucleus relativistic multiple scattering theory with delta degrees of freedom. Can. J. Phys. 91, 424-432.

Werneth, C. Norbury, J. Blattnig, S., 2013a. Pion cross section parameterizations for space radiation codes. Nucl. Instr. Meth. Phys. Res. B 298, 86-95.

Werneth, C.M., Maung, K.M., Mead, L., Blattnig, S.R., 2013b. Finite sum expressions for elastic and reaction cross sections. Nucl. Instr. Meth. Phys. Res. Res. B 308, 40-45.

Werneth, C.M., Maung, K.M., Ford, W.P., Norbury, J.W., Vera, M.D., 2014. Elastic differential cross sections for space radiation applications. Phys. Rev. C 90, 064905.

Werneth, C.M., Maung, K.M., Ford, W.P., 2015. Relativistic elastic differential cross sections for equal mass nuclei. Phys. Lett. B 749, 331-336.

Werneth, C.M., Xu, X., Norman, R.B., Ford, W.P., Maung, K.M., 2017a. Validation of elastic cross section models for space radiation applications. Nucl. Inst. Meth. Phys. Res. B 392, 74-93.

Werneth, C.M., Xu, X., Norman, R.B., Maung, K.M., 2017b. Relativistic three-dimensional Lippmann-Schwinger cross sections for space radiation applications. Nucl. Inst. Meth. Phys. Res. B 413, 75-78.

Wilson, J.W., Townsend, L.W., Badavi, F.F., 1987. Galactic cosmic ray propagation in Earth's atmosphere. Rad. Res. 109, 173-183.

Wilson, J.W., Townsend, L.W., Schimmerling, W., Khandelwal, G.S., Khan, F., Nealy, J.E., Cucinotta, F.A., Simonsen, L.C., Shinn, J.L., Norbury, J.W., 1991. Transport methods and interactions for space radiations. NASA Research Publication 1257, 1991.

Wilson, J.W., Shinn, J.L., Townsend, L.W., Tripathi, R.K., Badavi, F.F., Chun, S.Y., 1994. NUCFRG2: A semiempirical nuclear fragmentation model. Nucl. Instr. Meth. Phys. Res. B 94, 95-102.

Wilson, J.W., Tripathi, R.K., Badavi, F.F., Cucinotta, F.A., 2006. Standardized radiation shield design method: 2005 HZETRN. SAE/ICES paper 2006-01-2109.

Wilson, J.W., Nealy, J.E., Dachev, Ts.P., Tomov, B.T., Cucinotta, F.A., Badavi, F.F., De Angelis, G., Atwell, W., Leutke, N., 2007. Time serial analysis of the Induced LEO environment within the ISS 6A. Adv. Space Res. 40, 1562-1570.

Wilson, J.W., Slaba, T.C., Badavi, F.F., Reddell, B.D., Bahadori, A.A., 2014. Advances in NASA radiation transport research: 3DHZETRN. Life Sci. Space Res. 2, 6-22.

Wilson, J.W., Slaba, T.C., Badavi, F.F., Reddell, B.D., Bahadori, A.A., 2015a. 3DHZETRN: Neutron leakage in finite objects. Life Sci. Space Res. 7, 27-38.

Wilson, J.W., Slaba, T.C., Badavi, F.F., Reddell, B.D., Bahadori, A.A., 2015b. 3DHZETRN: Shielded ICRU spherical phantom. Life Sci. Space Res. 4, 46-61.

Wilson, J.W., Slaba, T.C., Badavi, F.F., Reddell, B.D., Bahadori, A.A., 2016. Solar proton exposure of an ICRU sphere within a complex structure: Combinatorial geometry. Life Sci. Space Res. 9, 69-76.

Wilson, J.W., Werneth, C.M., Slaba, T.C., Badavi, F.F., Reddell, B.D., Bahadori, A.A., 2017. Neutron angular scatter effects in 3DHZETRN: Quasi-elastic. NASA Technical Paper 2017-219597.

Xapsos, M.A., Summers, G.P., Barth, J.L., Stassinopoulos, E.G, Burke, E.A, 1999. Probability model for cumulative solar proton event fluences. IEEE Trans. Nucl. Sci. 46, 1481-1485.

Zeitlin, C., Guetersloh, S., Heilbronn, L., Miller, J., Fukumura, A., Iwata, Y., Murakami, T., Sihver, L., Mancusi, D., 2008a. Fragmentation cross sections of medium energy ^{35}Cl, ^{40}Ar, and ^{48}Ti beams on elemental targets. Phys. Rev. C 77, 034605.

Zeitlin, C., Sihver, L., La Tessa, C., Mancusi, D., Heilbronn, L., Miller, J., Guetersloh,

S., 2008b. Comparisons of fragmentation spectra using 1 GeV/amu ^{56}Fe data and the PHITS model. Rad. Meas. 43, 1242-1253.

Zeitlin, C., Guetersloh, S., Heilbronn, L., Miller, J., Fukumura, A., Iwata, Y., Murakami, T., Sihver, L., 2010. Nuclear fragmentation database for GCR transport code development. Adv. Space Res. 46, 728-734.

Zeitlin, C., Miller, J., Guetersloh, S., Heilbronn, L., Fukumura, A., Iwata, Y., Murakamiand, T., Blattnig, S., Norman, R., Mashnik, S., 2011. Fragmentation of ^{14}N, ^{16}O, ^{20}Ne, and ^{24}Mg nuclei at 290 to 1000 MeV/nucleon. Phys. Rev. C 83, 034909.